Universal Point of Care Biosensor using Ultrafast Plasmonic Polymerase Chain Reaction

Ngoc Anh Minh Tran

McGill University

supervised by
Dr. Andrew Kirk

January 19, 2018

Abstract

This thesis gives an overview of polymerase chain reaction (PCR) and where PCR is currently used in research and the industry. The thesis discusses the specific components and stages of PCR. It gives an overview of the chemistry, engineering and biology required to perform PCR in both real time and in gel electrophoresis. We go through the underlying laws of physics involved in direct non-contact heating, various thermometry techniques, and single input single output (SISO) control systems.

We investigate the inhibition properties of nanoparticles in PCR. With the inhibition concentration data, we determine the maximum absorbance per unit length of both nanoparticles to perform PCR. Using non-contact heating and non-contact thermometry, we explored the reliability of our PCR system and compared it to that of conventional Peltier elements used in research laboratories. We determine the optimal hold temperatures, and minimum hold time for both the annealing and denaturation stages.

We demonstrate a simplistic real-time and label-free method to monitor double stranded deoxyribonucleic acid production using only a ultraviolet (UV) LED and a UV photodetector, and compare it to that of tried and tested fluorescent-based quantitative PCR.

Sommaire

Ce mémoire donne une vue d'ensemble de l'amplification en chaîne de par polymérase (PCR) et de ses applications en recherche et en industrie. Il discute des composantes spécifiques et des étapes de la PCR et donne un aperçu des connaissances requises dans les domaines de la chimie, de l'ingénierie et de la biologie pour effectuer une électrophorèse sur gel et une PCR en temps réel. Nous abordons ensuite les lois de la physique qui sous-tendent le concept de chauffage direct sans contact, plusieurs techniques de thermométrie et les systèmes Single Input Single Output (SISO).

Nous examinons également les propriétés d'inhibition des nanoparticules présentes dans une PCR. Grâce aux données de concentrations d'inhibition, nous déterminons l'absorbance maximale par unité de longueur requise pour effectuer une PCR de chacun des deux types de nanoparticules étudiées. En utilisant des techniques de chauffage et de thermométrie sans contact, nous déterminons la fiabilité de notre système de PCR et la comparons à celle d'éléments de Peltier conventionnels utilisés dans les laboratoires de recherche. Nous déterminons ensuite la température de maintien optimale et le temps de maintien minimal pour les phases d'appariement et de dénaturation.

Puis, nous développons une méthode en temps réel sans marqueur de contrôle de la production d'acide désoxyribonucléique à double brins qui n'utilise qu'une diode émettant de la lumière ultraviolette et un photodétecteur de rayons ultraviolets. Finalement, nous comparons cette méthode à la technologie éprouvée de la PCR quantitative avec marqueurs fluorescents.

Acknowledgement

First, I would like to thank Mr Seung Soo Lee, without whose support this work would not have been possible. Seung repeatedly challenged me, making me think about things that would've seem trivial at first glance. He did the most important thing of all, which was to provide support as a drinking buddy. I would also like to thank Wenxuan Tang for helping out with the arduino code for the microcontroller.

I thank my thesis advisor Andrew Kirk, for introducing me to the project and allowing me the opportunity to work and learn. Eternal thanks to Mark Trifiro and Miltiadis Paliouras for their inputs and dedication to getting the project going.

Finally I would like to thank Yukiko Sato, Oulin Yu and Andrea Ngo as the second readers of this thesis. I am gratefully indebted to them for their very valuable comments on this thesis.

Contents

List of Figures

List of Tables

List of Abbreviations

AuNR	Gold Nanorods
BIBO	Bounded Input Bounded Output
BJT	Bipolar Junction Transistor
bp	Base Pairs
CT	Chlamydia Trachomatis
DAC	Digital to Analog Converters
DDA	Discrite Dipole Approximation
DNA	Deoxyribonucleic Acid
dNTP	Deoxynucleotide Triphosphates
dsDNA	Double Stranded Deoxyribonucleic Acid
FRET	Fluorescent Resonance Energy Transfer
LSPR	Localized Surface Plasmon Resonance
LTI	Linear Time Invariant
MIMO	Mutli Input Multi Ouput
MWCNT	Multi Wall Carbon Nanotubes
PCR	Polymerase Chain Reaction
PD	Propotional Derivative
PI	Propotional Integral
PID	Propotional Integral Derivative
qPCR	Quantitative Polymerase Chain Reaction
ssDNA	Single Stranded Deoxyribonucleic Acid
UV	Ultra Violet
LASER	light amplification by stimulated emission of radiation
SISO	Single Input Single Output
SP	Surface Plasmons
SPR	Surface Plasmon Resonance

Chapter 1

Motivation

1.1 PCR Applications

Polymerase chain reaction, more commonly referred to as PCR is a molecular biology technique drastically improved in 1985 by Kary B. Mullis, used to multiply a single copy or a few copies of a segment of DNA across several orders of magnitude, generating thousands to millions of copies of a particular DNA sequence [1]. His improvement of PCR won him the Nobel Prize in Chemistry in 1993.

1.1.1 Medical and Infectious Disease Applications

The first application of PCR is for genetic testing, where a sample of DNA is analyzed for the presence of genetic disease mutations [2]. Prospective parents can be tested to check whether they are genetic carriers, while their children can be tested to see if they have a genetic mutation. DNA samples for prenatal testing can be obtained by various methods, including amniocentesis. The latter is a process by which a small amount of amniotic fluid, which contains fetal tissues and therefore its DNA, is extracted from the mother.

Traditionally, tissue typing, a process which tests for compatability between prospective organ donors and recipients, is achieved through antibody-based tests for blood type. However, there has been a proposal to replace this method with PCR-based tests, due to PCR's simplicity relative to that of antibody-based tests [3].

An oncogene is a gene that has the potential to cause cancer. Many forms of cancer involve mutations of normal genes to oncogenes. By using PCR-based tests to study these mutations, therapy regimens can sometimes be individually customized to a patient. In addition, PCR permits early diagnosis of dangerous cancers such as leukemia and lymphomas [4]. PCR analysis can be performed directly on DNA samples to detect translocation-specific malignant cells at a sensitivity that is at least 10 000-fold higher than that of other methods [5].

According to the world health organizations, around 1 million individuals died in 2016 due to illnesses indirectly caused by HIV, with the overwhelming majority of cases occurring in developing nations such as Nigeria, South Africa and India [6]. Although HIV has been known since 1981, one of the reasons why it has not been eradicated yet is due to the fact that the current earliest HIV detection methods relies on the presence of antibodies to the

virus, which do not appear until many weeks after infection. PCR however, has been able to detect as little as one viral DNA copy of over 50 000 host cells [7], allowing for detection at a much earlier stage, and potentially, eradicating HIV.

Bacterial infections are typically diagnosed using cell culture or by growing the bacteria on agar plates. However, some bacterial infection such as tuberculosis are difficult to sample from patients and can take a while before detected by culture. PCR has allowed the diagnostic process for tuberculosis to be easily obtained and verified.

Antibiotic resistance has been a growing problem in hospitals and can drastically change the therapeutic approach towards the patient. PCR permits detecting the antibiotic resistance and allow patient specific treatement. Furthermore the effectiveness of the treatment could by anyalzed through PCR.

The ability to test for infections early on has prompted PCR to be used in the farming industry [8]. In dentistry, PCR plays an important role. Subgingival plaque, saliva, mouthwash, blood, gingival tissue, and buccal mucosa scraping are used in PCR to identify microorganisms, genetic polymorphisms, and mRNA gene expression of various inflammatory mediators in dentistry[9, 10].

1.1.2 Forensic Applications

Forensic DNA typing is an effective way of identifying or exonerating criminal suspects by analyizing the evidence discovered at a crime scene. The human genome has many repetitive regions that can be found within gene sequences or in non-coding regions of the genome. Specifically, up to 40% of human DNA is repetitive [11]. There are two distinct categories for these repetitive sections in the genome. The first category is called variable number tandem repeats (VNTR), which are composed of 10-100 base pairs and the second category is called short tandem repeats (STR) and these consist of repeated 2-10 base pair sections. PCR is used to amplify several well-known VNTRs and STRs using primers that flank each of the repetitive regions. The sizes of the fragments obtained from any individual for each of the STRs will indicate which gene variants are present. By analyzing several STRs for an individual, a set of gene variations that is statistically likely to be unique to each can be found [11]. Researchers have identified the complete sequence of the human genome. This sequence can be easily accessed through the National Center for Biotechnology Information website and is used in many real-life applications. For example, the FBI has compiled a set of DNA marker sites used for identification, and these are called the Combined DNA Index System (CODIS) DNA database [11]. Samples such as a single human hair attached to its hair follicle has enough DNA to conduct the analysis. Similarly, a few sperm cells, skin samples from under the fingernails, or a small amount of blood can provide enough DNA for a conclusive analysis [11].

1.1.3 Research Applications

Phylogenics is the study of the evolutionary history and relationships among individuals and or groups of organisms. Phylogenic analysis of ancient DNA sources, such as bones recovered from Neanderthals or from frozen tissues of mammoths can be performed. In some cases the highly degraded DNA from these ancient sources might be reassembled during the

early stages of amplification. Sequence-tagged sites is a process where PCR is used as an indicator that a particular segment of a genome is present in a particular clone. The Human Genome Project found this application vital to mapping and to the coordinating results from different laboratories of cosmid clones they were sequencing. A common application of PCR is the study of patterns of gene expression. Tissues (or even individual cells) can be analyzed at different stages to see which genes have become active, or which have been switched off. This application can also use quantitative PCR to quantitate the actual levels of expression. In fact, PCR is so common that it is now virtually impossible not to find a PCR thermocycler in a health-science related research institute.

1.2 PCR improvement

The mechanism of conventional PCR thermocyclers is mentioned in more detail in section 2.1.6. The current state-of-the-art PCR thermocycler, ProFlex PCR System, costs about $9250 CAD, at the time of writing, it can perform PCR between 20 to 40 minutes, depending on the length of DNA, and this device is anything but portable. There has been a very recent paper about a handheld real time PCR thermocycler [12]. It works with sample volumes in the hundreds of nanolitres, while taking 30 minutes for a complete PCR. Our goal is to develop a system which performs PCR in less than 10 minutes, with volumes between 10-25 microlitres while keeping the system compact, energy efficient, and at a low cost.

Chapter 2

Literature Review

2.1 Polymerase Chain Reaction Diagnostic

2.1.1 Deoxyribonucleic Acid

DNA or deoxyribonucleic acid is a molecule which carries genetic instructions used in the growth, development, functioning and reproduction of all known living organisms. DNA molecules consist of two biopolymer strands coiled around each other to form a double helix structure, see fig. 2.1. The two DNA strands are also called polynucleotides since they are

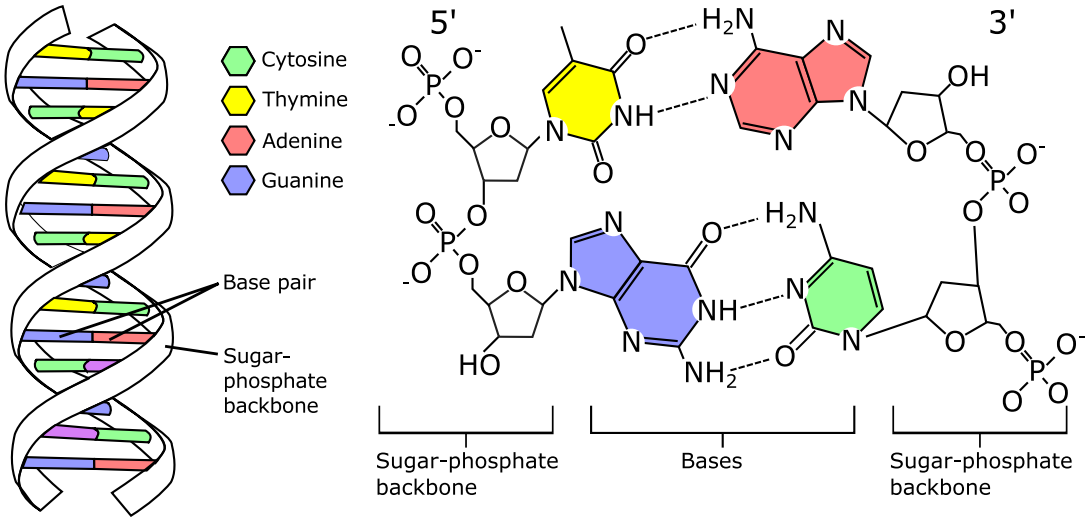

Figure 2.1: The structure of the DNA double helix. The atoms in the structure are colour-coded by element and the detailed structures of two base pairs are shown in the bottom right.

composed of simpler monomer units called nucleotides. Each of the nucleotides is composed of one of four nitrogen-containing nucleobases (cytosine (C), guanine (G), adenine (A), or thymine (T)), a sugar called deoxyribose, and a phosphate group (fig. 2.1).

The nucleotides are joined to one another in a chain by covalent bonds between the sugar of one nucleotide and the phosphate of the next, resulting in an alternating sugar-phosphate

backbone. This sugar phosphate backbone gives DNA its negative charge; the longer the DNA strand is, the more negatively charged the DNA becomes. The nitrogenous bases of the two separate polynucleotide strands are bound together according to base pairing rules (A with T, and C with G) with hydrogen bonds to make double-stranded DNA (dsDNA). DNA strands are assymetric in nature with one end classified as 5' and the other 3'. This indicates the carbon numbers in the DNA's sugar backbone. The 5' carbon has a phosphate group attached to it and the 3' carbon a hydroxyl (-OH) group. This asymmetry gives a DNA strand a "direction" [13].

The hydrogen bonds between the two DNA strands are weaker in comparison to the bonds between the nucleotides and can be easily broken with temperature. The process in which dsDNA turns into single-stranded DNA (ssDNA) is called the melting of DNA. The melting temperature T_m is the temperature in at which 50% of the DNA in a sample has denatured from dsDNA to ssDNA. There are many factors that effects the DNA's T_m, ranging from salt concentration, pH, the presence of DNA intercalators to aromatic compounds that can be toxic or mutagenic due to their ability to insert themselves between DNA bases. However, the two factors in which we are most interested are the number of nucleotide bases and the number of nucleotides bases that are either of type G or C. The first way in which the numbers of nucleotide bases would affect the melting temperature is rather intuitive. A higher number of base pairs means that more hydrogen bonds need to be broken in order to melt the DNA. In other words, longer DNA strands have a higher melting temperature, T_m [14]. The bond between the G and C bases are much stronger and thus for DNA strands of the same length, the DNA with more GC contents will have a higher melting temprature. This concept is shown in fig. 2.2, taken from [14].

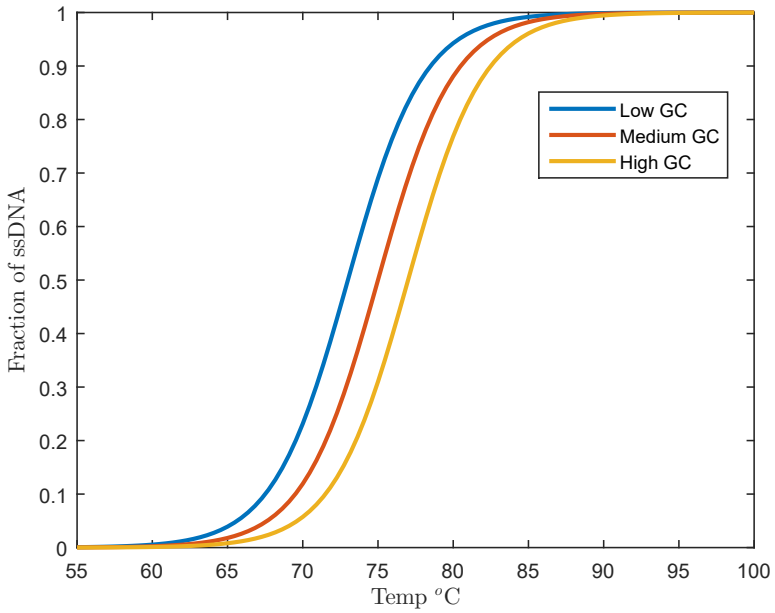

Figure 2.2: DNA melting curves for three strands of DNA with different levels of GC content. The y-axis indicates the fraction of DNA molecules that are single-stranded.

There are many approximate quantitative approaches for calculating the T_m of short DNA strands one of them being colloquially known as the "2-4 Rule" from [15], shown in eq. (2.1). This rule is valid for sequences less than 14 nucleotides, whereas for sequences longer than 13 nucleotides eq. (2.2) is more accurate. Both rule assume a DNA concentration of 50 nM, 50 mM of Na^+, and pH of 7.0.

$$T_m = (N_A + N_T) \times 2°\text{C} + (N_G + N_C) \times 4°\text{C}s. \tag{2.1}$$

$$T_m = 64.9°\text{C} + 41 \times (N_G + N_C - 16.4)/(N_A + N_T + N_G + N_C)°\text{C}. \tag{2.2}$$

Where in both eqs. (2.1) and (2.2), N_A, N_T, N_G and N_C refer to the number of A,T G and C nucleotides, respectively. As mentioned previously there are many other parameters that affect the T_m. For sequences longer than 50 base-pairs eq. (2.2) is no longer valid, and more complicated models which will not be discussed in this thesis would have to be invoked.

2.1.2 Polymerase Chain Reaction

Five main components are required for PCR to occur:

- **DNA templates** that contains the DNA target region to be amplified
- **dNTPs** or Deoxynucleotide triphosphates, the building blocks from which the DNA polymerase synthesizes a new DNA strand
- **DNA polymerases**: like DNA replication in an organism, PCR requires a DNA polymerase enzyme that makes new strands of DNA, using existing strands as templates.
- **DNA primers**: polymerase can only make DNA if it is given a primer, a short sequence of nucleotides that provides a starting point for DNA synthesis. In a PCR reaction, the experimenter determines the region of DNA that will be copied, or amplified by the primers that he or she designs.
- **A Buffer solution**, to ensure that the polymerase is in a suitable chemical environment.

Once all the components in their correct quantities are added to a reaction mixture, the next requirement is to control the PCR solution's temperature. Typically, PCR consists of a series of 20-40 repeated temperature changes, called cycles, with each cycle commonly consisting of two or three discrete temperature steps. The diagram for the reaction can be seen in fig. 2.3, and the steps for each cycle are as follows:

- **Denaturation** is the first regular cycling event and consists in heating the reaction at a high enough temperature to melt the template's DNA from dsDNA into ssDNA. The temperature needs to be as high as possible to maximize the fraction of ssDNA. However, temperatures too high can permanently destroy the polymerase, and preventing DNA from being replicated[16].

- **Annealing**, once the template's DNAs are in their single stranded form, primers need to anneal or hybridize to the template's DNAs. This temperature must be low enough to allow for hybridization of the primer to the strand, but high enough for the hybridization to be specific, i.e., the primer should bind only to a perfectly complementary part of the strand, and nowhere else. If the temperature is too low, the primer may bind imperfectly. If it is too high, the primer may not bind at all. Hence, it is critical to determine a proper temperature for the annealing process [17].
- **Elongation**, in this step the DNA primers that have been annealed to the DNA template will be elongated at the 5' end. For this reason, the temperature at this stage should that in which maximizes the polymerases' activity. This varies from one polymerase to another, but is usually around 72°C.

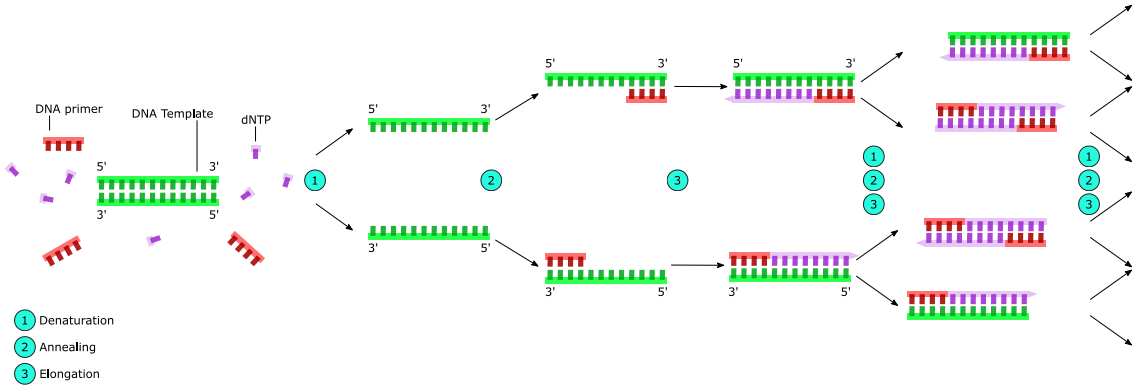

Figure 2.3: Schematic drawing of a complete PCR cycle.

We have so far only discussed the qualitative mechanisms of PCR. The true quantitative model under the surface is much, much more complicated and would itself be a reserach topic. Although annealing is by far the hardest PCR stage to model, it has been done and the full derivation can be found in [18]. To summarize, a DNA strand is considered high competing with high GC contents and low competing with low GC contents. It is favourable to get the hold time to be as long as possible at a fixed annealing temperature for low competiting DNA. However, for high competitng DNA, having the hold time too long reduces the efficiency.

2.1.3 Fluorescent Labels

In molecular biology and biotechnology, a fluorescent label, also known as a tag or probe, is a molecule that is attached chemically to aid in the labelling and detection of a biomolecule such as a protein, antibody, or amino acid. Generally, fluorescent labelling uses a reactive derivative of a fluorescent molecule known as a fluorophore. The fluorophore selectively binds to a specific region or functional group on the target molecule and is usually attached chemically [19]. Various labeling techniques such as enzymatic labeling, protein labeling, and genetic labeling are widely utilized. Ethidium bromide, for example, is a common tag, which are used in almost all labs in which PCR is conducted, due to its relatively low price.

Ethidium Bromide

When excited with UV-light of about 270nm-280nm, ethidium bromide fluoresces with an orange colour at 605 nm, intensifying almost 20-fold after intercalating between dsDNA. The hydrophobic environment found between the DNA base pairs is believed to be responsible for the increase in fluorescence. By moving into this hydrophobic environment and away from the solvent, the ethidium cation is forced to shed any water molecules that were associated with it. As water is a highly efficient fluorescent quencher, the removal of these water molecules allows the ethidium to fluoresce [20]. Since the vast majority of fluorescent intensity is due to dsDNA, fluorescent intensity is often approximated to being linearly dependant to number of dsDNA and hence our DNA product is commonly used.

PicoGreen

PicoGreen is an asymmetrical cyanine dye developed by Molecular Probes Inc., a wholly owned subsidiary of Life Technologies Corporation. It is marketed as being more sensitive and can detect "as little as 25 pg/ml of dsDNA in the presence of ssDNA, RNA, and free nucleotides"[21].

Similar to ethidium bromide, picogreen will fluoresce with a higher intensity in the presence of dsDNA; however the absorption and emission peaks are at 485 nm and 520 nm respectively. Little is known about the exact science behind the florescence property of picogreen as it is a well-kept secret.

Theoretically, the numbers of DNA copies would increase exponentially as a function of the number cycles. This assumption however does not take into consideration the reduction in efficiency of DNA polymerase due to temperature [16], and reduction in the number of primers, as they are extended into DNA products. In reality, the number of DNA copies increases exponentially for the first few cycles and saturates above 35 to 40 cycles. An example of DNA product as a function of the number of cycles can be seen in fig. 2.4.

2.1.4 DNA Gel Electrophoresis

Electrophoresis is the motion of dispersed particles relative to a fluid under the influence of a spatially uniform electric field. This phenomenon was observed for the first time in 1807 by Russian professors Peter Ivanovich Strakhov and Ferdinand Frederic Reuss, who noticed that the application of a constant electric field caused clay particles dispersed in water to migrate [22].

Assuming a low Reynolds number and a moderate electric field strength E, the drift velocity, which can be thought of as the speed at which a particle moves, v is simply proportional to the applied field, which is defined as the electric mobility μ_e. Thus, mathematically we have

$$\mu_e = \frac{v}{\mathrm{E}}. \tag{2.3}$$

The most well-known and widely used theory of electrophoresis was developed in 1903 by Smoluchowski [23], which predicts the mobility to be

$$\mu_e = \frac{\epsilon_r \epsilon_0 \zeta}{\eta}, \tag{2.4}$$

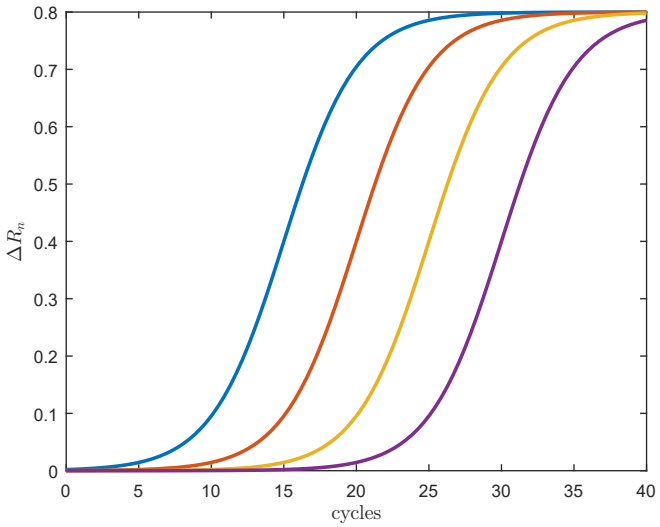

Figure 2.4: ΔR_n represents the change in fluorescence which is linearly dependent on the numbers of dsDNA, each colour represents a different starting template DNA concentration.

where ϵ_r is the dielectric constant of the dispersion medium, ϵ_0 is the permittivity of free space, η is the dynamic viscosity of the dispersion medium, and ζ is the zeta potential. Since the length of the DNA strand affects its overall charge, ζ and in turn μ_e will also be a function of DNA length. The actual length dependancy of the electric mobility (from [24]) is

$$\mu = \frac{1}{\beta + \alpha(1 - e^{-L/\gamma})}. \tag{2.5}$$

The values for β, α and γ from [24] is used to give us the plot for mobility as a function of length in fig. 2.5. For a constant electric field, shorter DNA strands will move faster than long DNA strands, which gives us the separation shown in fig. 2.7, for the first well, which contains DNA stands of various sizes.

Gel electrophoresis is a more specific form of electrophoresis in which particles are made to move through a gel made of agar or polyacrylamide instead of a fluid, which ensures that the particles stay in place after the electric field has been turned off. Hence, by introducing a fluorescent such as ethidium bromide into a gel mixture such as agar gel, is is possible to ensure that the DNA product is present and is of the correct length, and thereby verify that PCR has occurred as intended. An illustration of DNA electrophoresis is shown in fig. 2.6. Completed PCR mixtures are loaded into the wells or "sample wells" in fig. 2.6 together with a ladder, a mixture with DNA of different sizes to estimate the length of the DNA product. The power supply is turned on, creating an electric field [25]. fig. 2.7 shows an example of completed ethidium bromide electrophoresis gel under a UV lamp.

2.1.5 Real-time PCR

Despite its robust use and impact on biology, traditional PCR has limitations. A real-time polymerase chain reaction, also known as quantitative polymerase chain reaction (qPCR) is

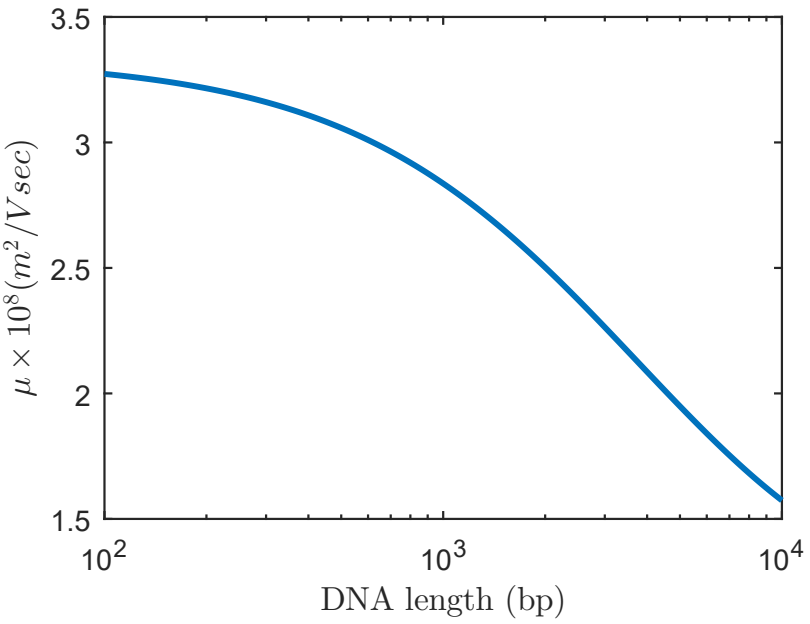

Figure 2.5: Representative dependencies of DNA mobilities on length [24].

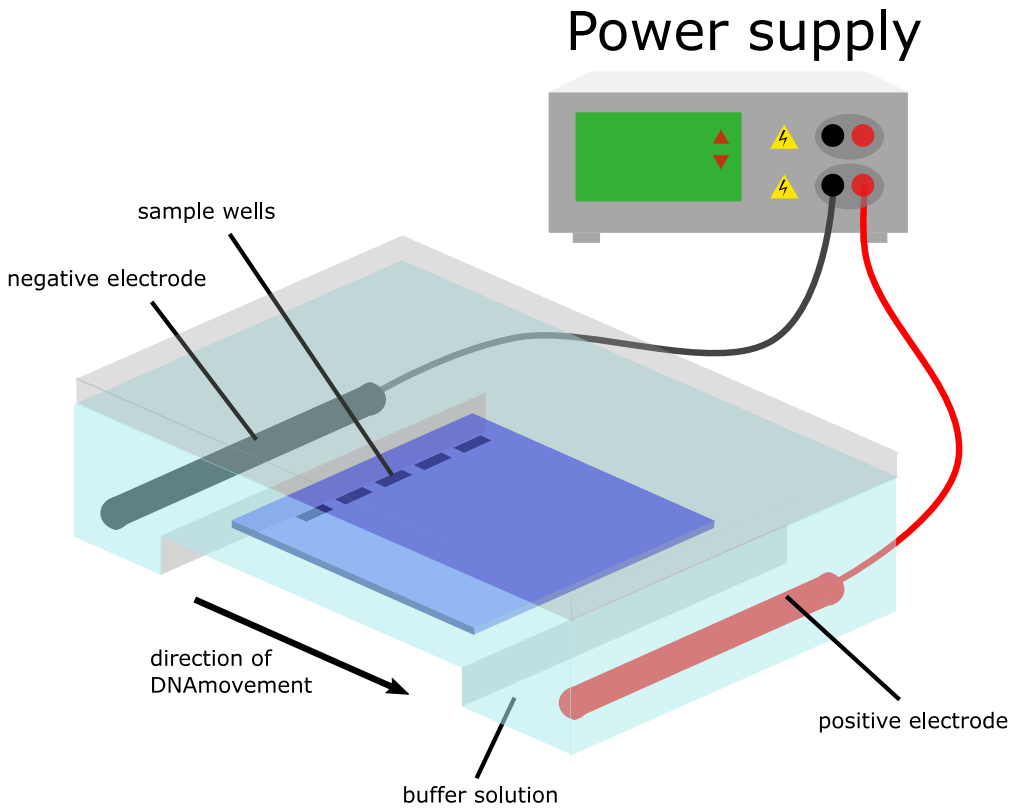

Figure 2.6: Illustration of DNA electrophoresis equipment used to separate DNA fragments by size.

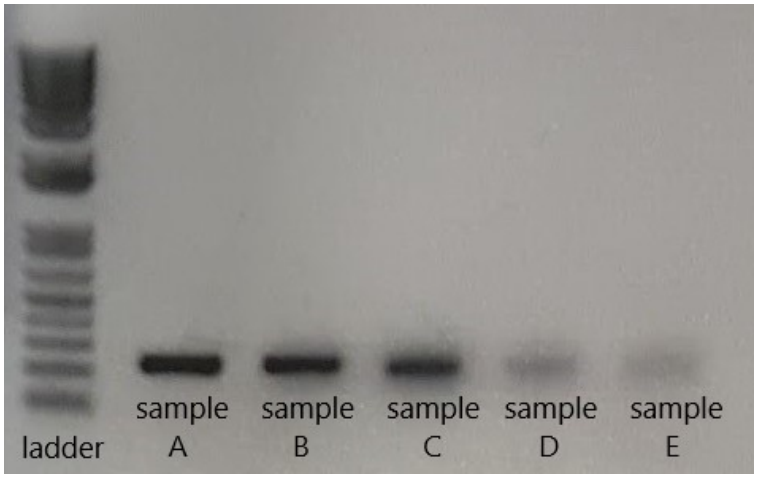

Figure 2.7: Different PCR samples of completed electrophoresis gel.

an add-on feature for PCR. qPCR techniques monitor the amplification of a targeted DNA molecule during the PCR, i.e. in real-time and not at the end of the reaction.

Fluorescent labels

Fluorescent labels can be added directly into the PCR mix to measures its fluorescent signal at each cycle. Fluorescent DNA-intercalating dyes such as ethidium bromide are a simple and straightforward compound, which can be used in qPCR. In fact, the first qPCR assays employed ethidium bromide as a detection mechanism, as it also binds the double-stranded DNA produced during amplification. However, concerns over safety and sensitivity of ethidium bromide led to the use of alternative fluorescent intercalating dyes, including SYBR/pico Green Dye, in the qPCR reaction. Like ethidium bromide SYBR/Pico Green preferentially binds to double-stranded DNA, but with a much greater affinity. The use of SYBR green and pico green has improved the sensitivity of detection meaning that fewer PCR cycles are required. These dyes are also far more quantitative, as the emission of fluorescence is directly proportional to the amount of PCR product generated [21].

Fluorescent Resonance Energy Transfer Probes

The most common probe format is the dual-labeled probe, which is a DNA strand containing a reporter fluorophore that emits a signal at the 5' end and a quencher at the 3' end to extinguish the reporter fluorescence when it is not bound to the target DNA. The fluorescent reporter dye becomes excited at a specific wavelength and emits energy in the form of light with a longer wavelength. However, when the excited reporter dye is in close proximity to a quencher dye, which has an overlapping absorption spectrum, this light energy is transferred to the quencher instead. The light energy is then dissipated at the emission of the quencher, allowing the fluorophore to return to the ground state without releasing photons. This conversion of energy to the quencher is known as fluorescent resonance energy transfer (FRET).

There are typically two main mechanisms that allow the fluorescence of the probe:

1. **Hybridization to target**- Before binding to the target DNA the probe is in its single-stranded form, which makes it very flexible and thus often bent. Hence, the fluorescent end of the probe and the quencher end of the probe are often in close proximity and thus no flourescent signal can be observed. However, when the probes bind to the target DNA forming partial dsDNA, the binding process linearizes the probe and increases the distance between the fluorophore and the quencher. The fluorescent reporter signal can then be emitted because the distance has increased between the two dye molecules on the probe. During a PCR cycle, the binding of the probe will occur during annealing. The process is shown in fig. 2.8.

2. **Cleavage by polymerase**- For these type of probes, the fluorescing light signal from the probe is further enhanced when Taq polymerase cleaves the fluorophore off the probe using its 5'-3' exonuclease activity. The hydrolysis event permanently separates the fluorophore from the quencher and the two entities are no longer linked (fig. 2.9). If the polymerase does not cleave the probe, it is simply displaced during extension and can re-enter its quenched state ready to participate in the next cycles. These two mechanisms operate together to create a robust signal during the reaction. Because of the additional cleaving the fluorescent curve would look as represented in fig. 2.10.

Nucleic Acid Optical Absorption

Due to their heterocyclic rings, nucleotides absorb UV light. Although each nucleotide type has a different spectrum (shown in fig. 2.11), where the data is taken from [27], these spectra average out to an absorption spectrum which has a maximum absorption at 260 nm. Free floating nucleotides that are not connected together have an average extinction coefficient of $10750 M^{-1} cm^{-1}$. After forming ssDNA the extinction coefficient decreases by approximately 10%, depending on the DNA sequence, due to base stacking limiting the resonance of heterocyclic rings. In double-stranded form, the stacking interactions are further enhanced due to the hydrogen bonds and hydrophobic effect between the complementary bases. This bond further limits the resonance of the heterocyclic rings [28]. The process by which the extinction coefficient at 260 nm is decreased, going from ssDNA to dsDNA is called hyperchromicity. Extinction coefficient for different form of nucleic acids are summarized in table 2.1. Measuring the absorption at 260 nm is one way, curves in fig. 2.2 are obtained.

There is however one slight problem with using 260 nm UV light to monitor PCR product. UVC (100 nm-280 nm) light is known to damage DNA: in fact, exposing DNA to both UVC and UVB (280 nm-315 nm) light forms pyrimidine dimers [29]. Pyrimidine dimers occur when there are two adjacent thymine base pair in a DNA sequence. Exposure to UV light causes the two thymine base pairs to link up through covalent bonding. Depending on the covalent bond, the two thymine base pair can form either a 6-4 product(left of fig. 2.12) or a cyclobutate (right of fig. 2.12). The formation of these pyrimidine dimers causes a kink in the DNA sequence. Depending on the intensity of the UV radiation and exposure time, dsDNA might not form at all.

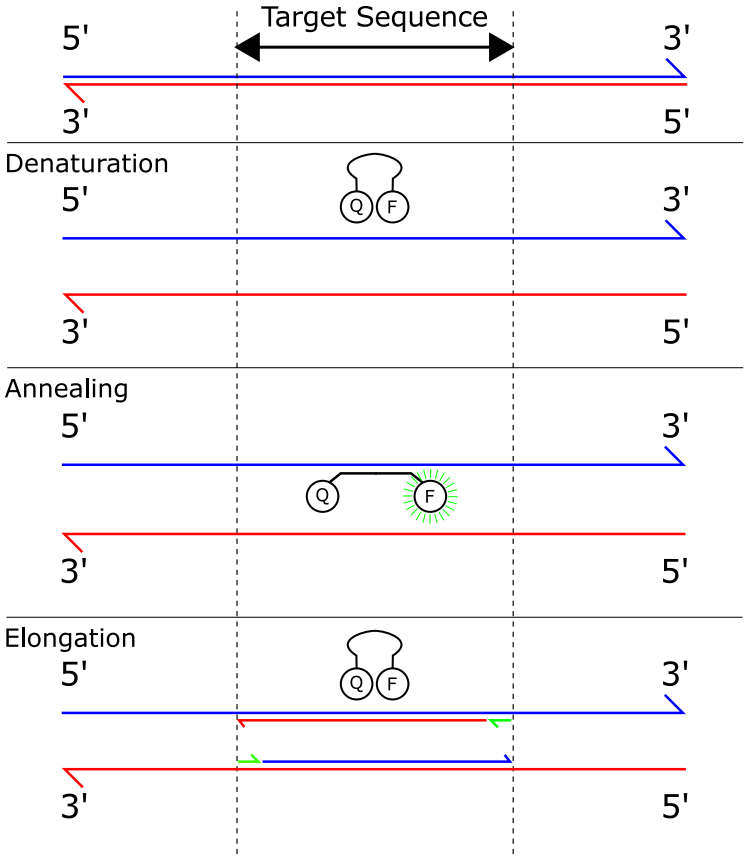

Figure 2.8: Illustration of how hybridizing probes fluoresce throughout PCR cycles.

	Average Extinction Coefficient at 260 nm
Free Nucleotides	10750 $M^{-1}cm^{-1}$
Nucleotides in ssDNA	9675 $M^{-1}cm^{-1}$
Nucleotides in dsDNA	7062 $M^{-1}cm^{-1}$

Table 2.1: Change of extinction coefficient of nucleotides in free, ssDNA and dsDNA form.

2.1.6 Contemporary PCR Machines

The Peltier block or element is one of the most commonly used heating elements in traditional PCR instruments [30, 31, 32]. The thermoelectric heating element gets its name from the Peltier thermoelectric effect. The Peltier effect is the opposite of the Seebeck effect, named after Thomas Johann Seebeck. According to the Seebeck effect, if different metals are connected in two separate places and the intersections are kept at different temperatures,

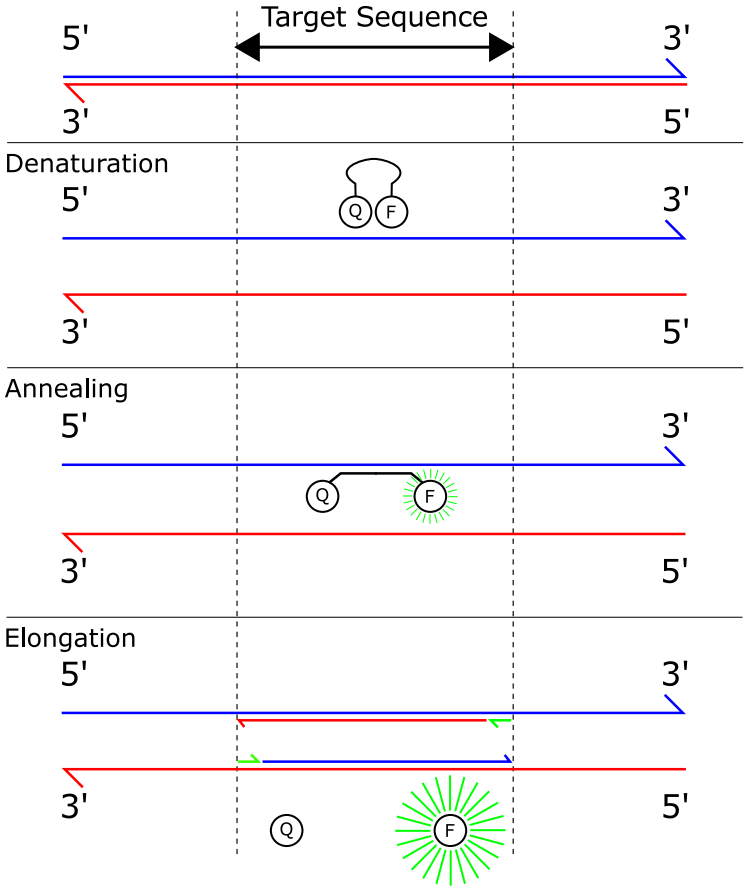

Figure 2.9: Illustration of how cleaving probes fluoresce throughout PCR cycles.

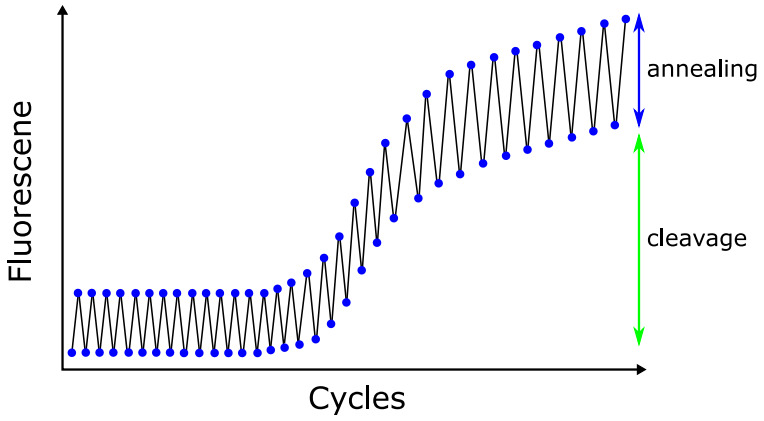

Figure 2.10: Visual representation of both probe annealing and cleavage occurring during a PCR reaction.

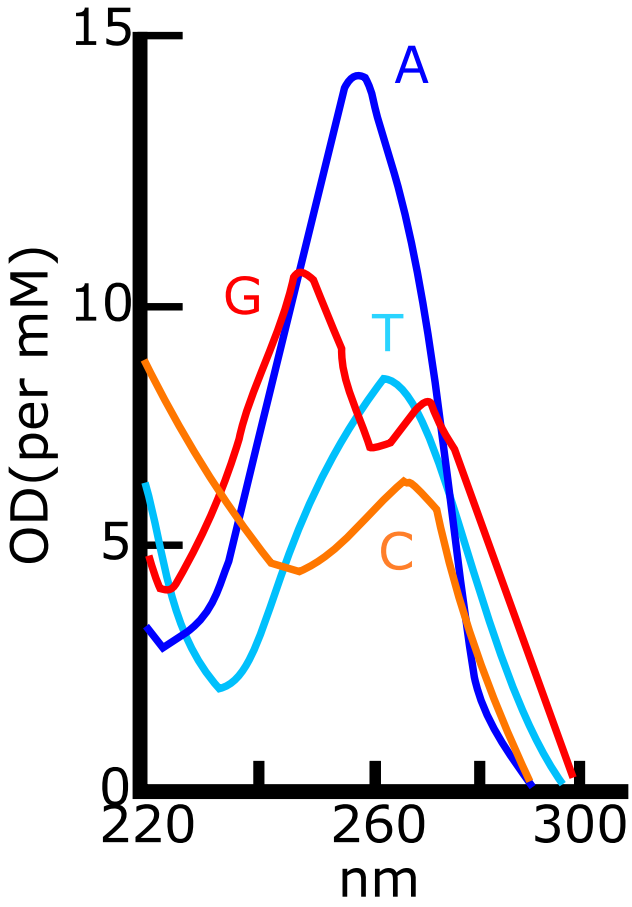

Figure 2.11: UV spectral absorption of nuclaic acid.

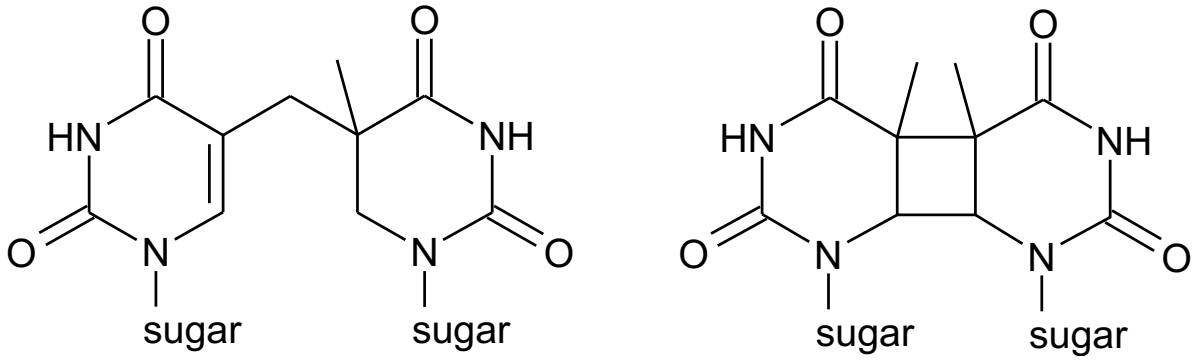

Figure 2.12: Molecular structure of thymine photodimer: 6,4-photoproduct (left) and cyclobutane.

then there will be a potential difference between the two junctions.

Later, in 1834, Jean Peltier found that the opposite of the Seebeck effect is also true: a potential difference can cause a temperature difference, regardless of what the ambient temperature is. Modern day semiconductor Peltier elements use a large number of n-type and p-type semiconductors see, fig. 2.13. When a DC current flows through the Peltier element,

it becomes a heat pump. In one polarity, heat will be pumped from the bottom to the top of the Peltier, allowing a sample to be heated. When the current is reversed, heat is pumped from the top to the bottom, allowing a sample to be cooled. Peltier elements are typically used in a configuration similar to that shown in fig. 2.14. In traditional instruments, as the Peltier element changes temperature, heat is transferred to the thermal interface, then to the heat spreader, then to the sample tube, and finally to the liquid in the reaction chamber.

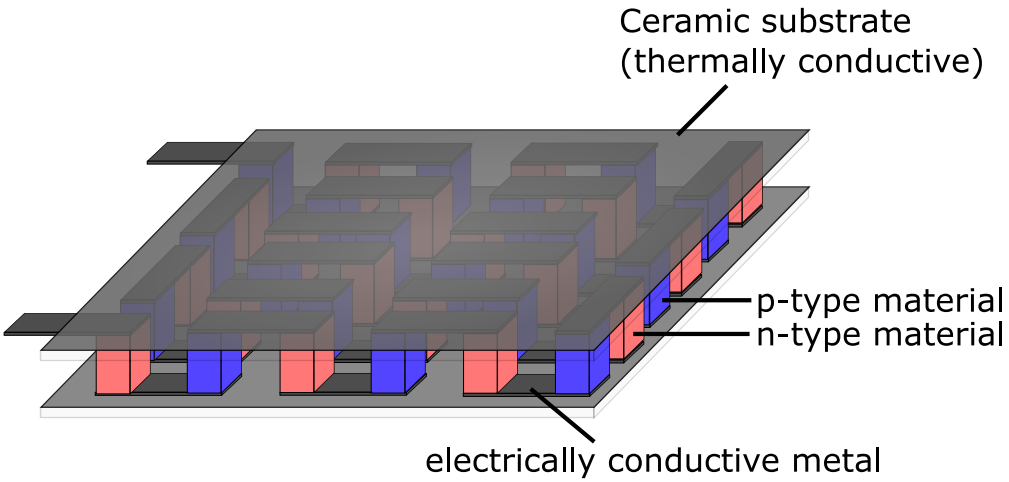

Figure 2.13: Structural diagram of a Peltier element.

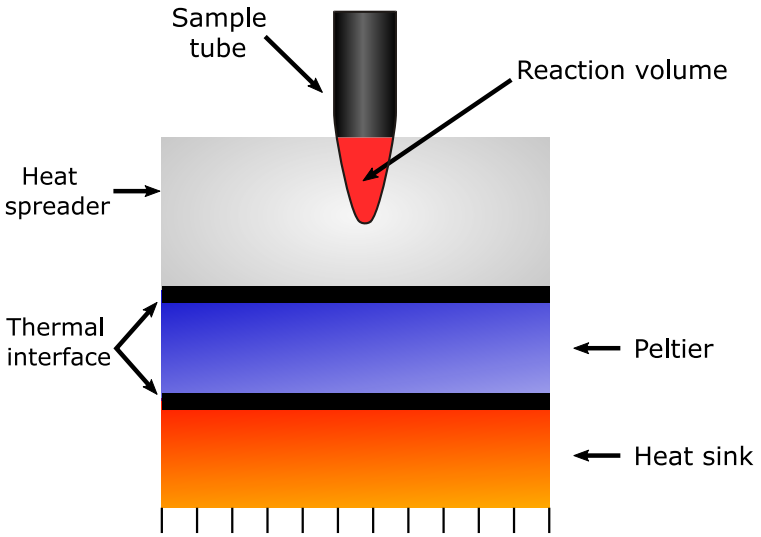

Figure 2.14: Example of a Peltier element in a traditional nucleic acid thermocycler. The heat is conducted from the Peltier across the thermal interface, into the heat spreader, to the reaction tube, and then to the reaction volume.

The advantages of Peltier elements are that the technology is well understood, thoroughly tested, and Peltier elements are readily available off-the-shelf at a low cost. One disadvantage of Peltier modules for use in PCR is that they may be relatively slow when working with microliter reaction volumes, as the entire Peltier element, heat spreader and reaction sample's

temperature must be changed at each cycle. The use of a water bath in conjunction with a robotic arm can be used to speed up the process. This, however, will increase cost, complexity and is certainly not a portable system. Moving to direct non-contact methods, which rely on electromagnetic radiation as the mechanism for heat transfer, can potentially address the shortcomings of contemporary PCR machines. One caveat of these non-contact heating is the wall-plug efficiency is typically not 100%. As an example, lasers have a wall plug efficiency of about 40-50%. A thorough analysis of heating efficiency taking into account wall-plug efficiency of non-contact vs contact heating method could be, but will not be performed in this thesis.

2.2 Non-Contact Heat Generation

Moving to direct non-contact methods which rely on electromagnetic radiation as the mechanism for heat transfer, can potentially address the shortcomings of contemporary PCR machines, by bypassing the heating elements. One caveat of these non-contact heating is the wall-plug efficiency is typically not 100%. As an example, lasers have a wall plug efficiency of about 40-50%. A thorough analysis of heating efficiency taking into account wall-plug efficiency of non-contact vs contact heating method could be, but will not be performed in this thesis. The following describes the mathematical model used for electromagnetic heating.

From the Beer-Lambert Law, the transmittance of an electromagnetic wave through a medium or solution is

$$T = \frac{P_{out}}{P_{in}} e^{-\mu c l}, \tag{2.6}$$

where P_{in} and P_{out} are the power of the electromagnetic wave before and after entering the solution respectively, μ is the attenuation coefficient per unit concentration-length, c is the molar concentration of the sample, and l is the optical path length of the medium. Assuming that a fraction of this power is transferred into heat,

$$Q_{in} = (P_{in} - P_{out})\eta = P_{in}(1 - e^{-\mu c l})\eta. \tag{2.7}$$

Where η is the heat conversation efficiency, which can be assumed to be ≈ 1 for the examples in this thesis. From the first law of thermodynamics,

$$\sum_i m_i C_{p,i} \frac{dT}{dt} = Q_{in} - Q_{out}, \tag{2.8}$$

where m_i and $C_{p,i}$ are the mass and heat capacity components of our solution. For the cases examined in this thesis, water will be the dominant component and $\sum_i m_i C_{p,i} \approx m_w C_w$, the product of mass and heat capacity of water. T is the temperature, t is time. Q_{out} is the heat leaving the solution. Heat can radiate away through black body radiation or by convection thus,

$$Q_{out} = S(h(T - T_o) + \epsilon\sigma(T^4 - T_o^4)), \tag{2.9}$$

where h is the heat transfer coefficient, S is the cross-sectional area perpendicular to the outward heat flow, ϵ is the emissivity of the material, σ is the Stefan-Boltzmann constant and

T_o is the ambient temperature. Comparing the heat flux (fig. 2.15) for materials between 21°C to 100°C, with the ambient air temperature at 21°C, convection is the dominant contributor to heat loss.

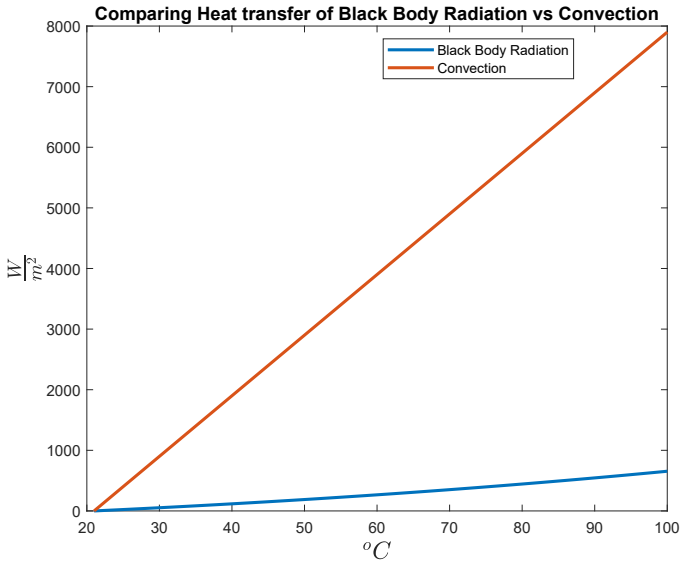

Figure 2.15: Comparing black body radiation to convection heat transfer in air.

Thus, we can approximate

$$Q_{out} \approx hS(T - T_o), \tag{2.10}$$

eq. (2.8) can then be re-written and approximated to be

$$m_w C_w \frac{dT}{dt} = P_{in}(1 - e^{-\mu cl}) - hS(T - T_o), \tag{2.11}$$

solving eq. (2.11), with the assumption $T(0) = T_o$, the ambient air temperature. The temperature as a function of time is

$$T(t) = T_o + \frac{P_{in}(1 - e^{-\mu cl})}{hS}\left(1 - exp\left(-\frac{hs}{m_w C_w}t\right)\right). \tag{2.12}$$

If $P_{in} = 0$ or if there is no radiation source, we have

$$T(t) = T_o + (T(0) - T_o)exp\left(-\frac{hs}{m_w C_w}t\right). \tag{2.13}$$

2.2.1 Liquid Water Absorption

For liquid water, the density will stay relatively constant and hence the concentration will also be relatively constant. This is why when discussing Beer-Lambert law for liquid water the μc parameter in eq. (2.6) can be combined into one variable, the absorption coefficient α_{H2O}. The plot of this α_{H2O} as a function of wavelength is shown in fig. 2.16.

Figure 2.16: Liquid water absorption spectrum from Deep UV to far-Infrared [33].

Although the absorption coefficient of water is at its greatest in the UV spectrum, this spectrum cannot be used to generate heat in PCR reactions as UV sources are very inefficient, and UV light itself can damage DNA[34]. Infrared sources can be and have been used for heat generations in PCR reactions [35]. Although the absorption coefficient of water is not as high in the microwave region, a strong case can still be made for using microwave sources to generate heat. Microwave sources are in general cheaper, more efficient, and they have also been used to drive PCR reactions [36]. However, there are no coherent microwave sources. While shaping the optical radiation of light can be done easily with a lens, doing the same for microwave radiation is not as simple.

2.2.2 Nano Particles Absorption

Local Surface Plasmon Resonance

Surface plasmons (SPs) are coherent electron oscillations that exist at the interface between any two materials where the real part of the dielectric function has different signs across the interface. Typically, the main component of solvents is water which has a positive dielectric constant. This dictates that the other medium must have a negative dielectric constant, which is why metals are often chosen as the other medium to support plasmons oscillations. The electromagnetic field intensity decays of exponentially from the interface, this is shown in fig. 2.17. The effective photon momentum at the surface boundary is given by

$$p_{eff} = \frac{h}{\lambda} n_m sin\theta, \tag{2.14}$$

where λ is the photon wavelength in vacuum, n_m is the refractive index of the medium, and θ is the angle of incidence. This effective momentum must match that of the surface plasmon momentum to transfer the incident lights energy to plasmonic oscillation at the surface. For

a fixed angle of incidence, we can describe the resonance wavelength as

$$\lambda_{res} = \frac{h}{p_{plasmon}} n_m sin\theta. \tag{2.15}$$

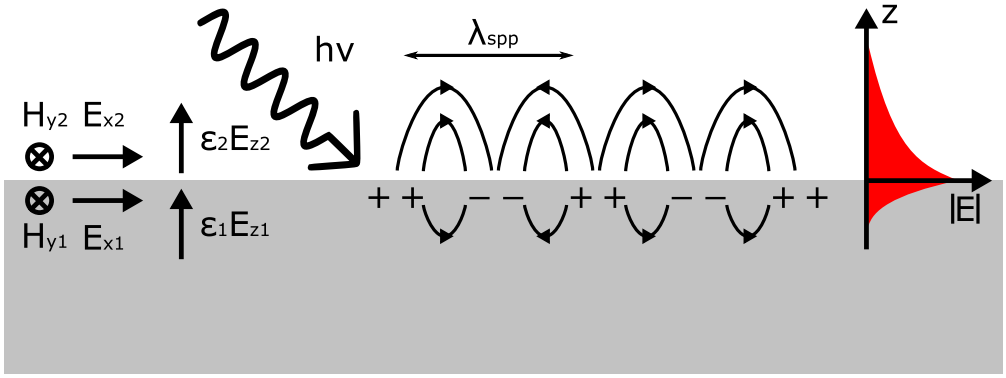

Figure 2.17: Schematic representation of an electron density wave propagating along a metal – dielectric interface. The charge density oscillations and associated electromagnetic fields are called surface plasmon-polariton waves. The exponential dependence of the electromagnetic field intensity on the distance away from the interface is shown on the right in red.

Localized surface plasmon Resonance (LSPR) occurs due to the confinement of a surface plasmon in a nanoparticle of size comparable to or smaller than the wavelength of light used to excite the plasmon. In 1912, Gans predicted that for very small ellipsoids, where the dipole approximation is satisfied, the surface plasmon mode splits into two distinct modes [37]. According to Gans's formula the polarizability of an elliopsoid along the three x,y,z axes are:

$$\alpha_{x,y,z} = \frac{4}{3}\pi abc \frac{\epsilon_m - \epsilon}{\epsilon_m + L_{x,y,z}(\epsilon_m + \epsilon)}. \tag{2.16}$$

Where a, b and c refer to the length of the ellipse along the x, y and z axes, with $a > b = c$. ϵ_m is the dielectric function of the metal, ϵ is the dielectric constant of the medium and $L_{x,y,z}$ is the depolarization factor for each axis given by:

$$L_x = \frac{1-e^2}{e^2}\Big(\frac{1}{2e} ln \frac{1+e}{1-e} - 1\Big), \tag{2.17}$$

$$L_{y,z} = \frac{1 - L_x}{2}. \tag{2.18}$$

Where e is the rod's geometric ellipticity given by $e^2 = 1 - (b/a)^2$. For a sphere $e = 0$, and the polarizability becomes:

$$\alpha_{sphere} = 3V \frac{\epsilon_m - \epsilon}{\epsilon_m + 2\epsilon}. \tag{2.19}$$

In eq. (2.6) the absorbance is written with the concentration in units of molarity. One could also rewrite the absorbance, $A = \sigma_{ext} Cl$, where now the concentration C, is expressed

as particle number density, σ_{ext} is known as the scattering cross section. Because gold nanoparticles do not emit light, we have

$$\sigma_{ext} = \sigma_{abs} + \sigma_{scattering}, \tag{2.20}$$

we can also define the scattering efficiency as

$$\eta = \frac{\sigma_{scattering}}{\sigma_{abs}}, \tag{2.21}$$

where the relation of extinction cross section and the polarizability in eq. (2.16) is

$$\sigma_{ext} = kIm(\alpha), \tag{2.22}$$

and the relation of scattering cross section with polarizability is

$$\sigma_{scattering} = \frac{k^4}{6\pi}|\alpha|^2. \tag{2.23}$$

Subtracting eq. (2.23) from eq. (2.22) gives us the absorbance cross section

$$\sigma_{abs} = kIm(\alpha) - \frac{k^4}{6\pi}|\alpha|^2. \tag{2.24}$$

Assuming that there are N randomly oriented ellipsoids using eq. (2.22) and summing all the contributions in x,y,z we get the extinction coefficient to be:

$$\gamma = \frac{2\pi NV\epsilon^{3/2}}{3\lambda} \sum_{x,y,z} \frac{\frac{1}{L_{x,y,z}^2}\epsilon_{m2}}{\left(\epsilon_{m1} + \frac{1-L_{x,y,z}}{L_{x,y,z}}\right)^2 + \epsilon_{m2}}, \tag{2.25}$$

where V is the particle volume, and ϵ_{m1} and ϵ_{m2} are the real and imaginary components of the dielectric function of the nanoparticles. The plot of eq. (2.24) is shown in fig. 2.18. Two local maxima can be seen in fig. 2.18 due to the transverse and resonance modes. The longitudinal excitation is much more sensitive to the aspect ratio

$$R = \frac{L}{W},$$

where L is the length and W is the width. fig. 2.18 shows that the absorbance of the longitudinal mode is much higher than that of the transverse mode. Thus, one could engineer the longitudinal mode to very strongly absorb anywhere between 530-1200 nm. The relationship between the longitudinal resonance mode and aspect ratio is shown in eq. (2.26).

$$\lambda_{LongRes} = 96R + 418\text{nm}. \tag{2.26}$$

The plot of eq. (2.26) (shown in fig. 2.19) is in good agreement with that of the discrete dipole approximation simulation [38], and the experimental data of Al-Sayed et al [39], and Perez-Juste et al [40].

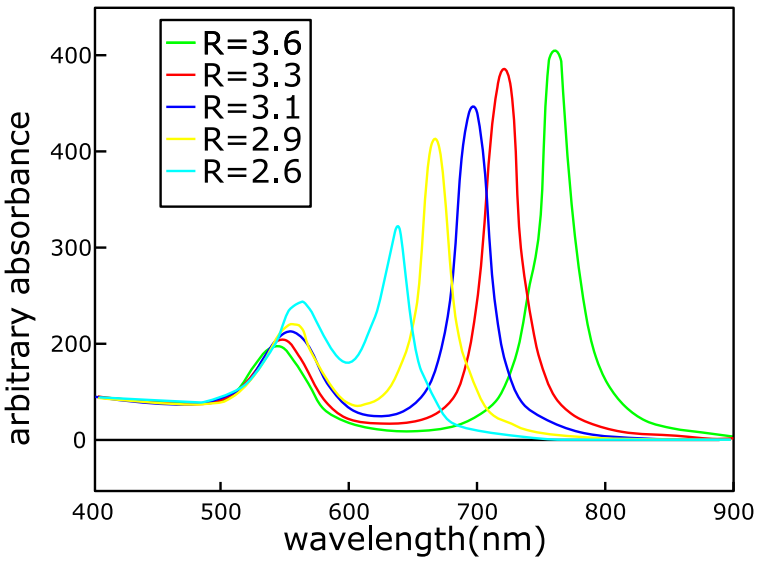

Figure 2.18: Calculated absorption spectra of elongated ellipsoids with varying aspect ratios R. The medium dielectric constant was fixed at a value of 4. The shorter wavelength peaks corresponds to the transverse mode resonance, and the longer wavelength peak to the longitudinal resonance which is very sensitive to the aspect ratio R.

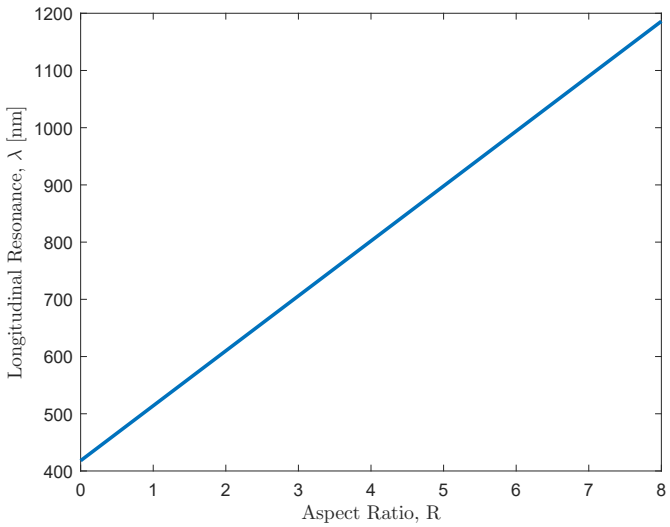

Figure 2.19: Position of longitudinal resonant wavelength versus the aspect ratio of nanorods.

One factor which contributes the popularity of gold nanorod is its interaction efficiency with light, with a ratio of extinction cross section to physical cross section greater than 1 (eq. (2.25)). The absorptive process which occurs on the order of 10-100 femtoseconds, is due to the creation of electron-hole pairs via either intraband excitations within the conduction band, or interband transitions from lower-lying d-bands to the sp-conduction [41]. In contrast, scattering occurs on the order of tens of femtoseconds and arises from the coherent oscillation of electrons [41]. After close inspection of eq. (2.23) and eq. (2.24), we see that the

scattering cross section has a volume squared dependence ($\sigma_{scattering} \approx V^2$) while the absorption cross section has a volume minus volume squared dependence ($\sigma_{abs} \approx (V - V^2)$). This suggests that larger nanoparticles would be preferred for plasmon enhanced fluorescence and imaging applications where the scattering component is critical. In contrast, smaller particles optimize the effectiveness of nonradiative processes, such as photothermal conversion for therapeutics or to drive PCR.

Because gold nanoparticles in general have a very low optical quantum yield, or in other words they very rarely emit light [42], almost all the absorbed energy to be converted into heat. The absorption coefficient can be as high as 140 cm^{-1} even for concentrations in the nanomolar range. Although LSPR is observed in both gold and silver, silver nanoparticles have been known to be quite toxic [43]. In addition, the production of gold nanorods has been established to the point in where they can be obtained off the shelves.

Carbon Nanotubes

In addition to gold antiparticles, carbon nanotubes have also been used for processes that require phothermal conversion. Carbon nanotubes are tubes made from folded graphene (a single layer of graphite). Depending on how the graphene is folded, carbon nanotubes can either be metallic or semiconducting with energy vs density of state relation shown in fig. 2.20.

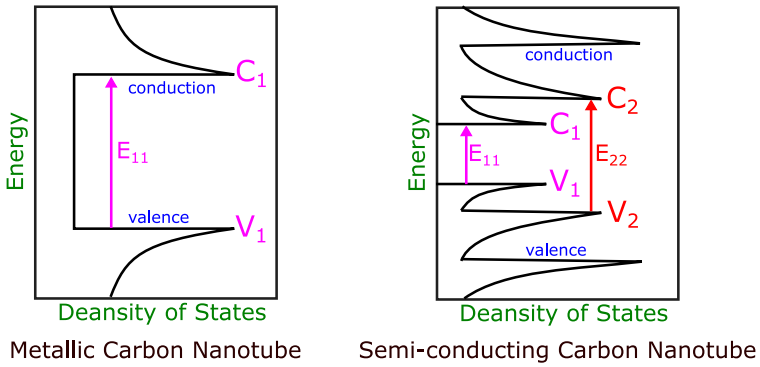

Figure 2.20: Typical densities of states as a function of energy for metallic and semiconducting single-wall carbon nanotubes.

The first and second Van Houve optical transitions are responsible for carbon nanotubes absorption peaks. The E_{11} and E_{22} energy transitions correspond to the first and second Van Houve optical transitions in fig. 2.20. Multi wall carbon nanotubes or MWCNT have been used to ablate prostate cancer cells by converting 532nm laser light into heat and locally coagulate the cancer cell [44].

Inhibition Properties

Adding nanoparticles however comes at a cost. Although the exact mechanism governing how the nanoparticles interact with the PCR component(s) is not well understood, we do know that there is a threshold of nanoparticle concentration which will inhibit PCR. We will explore this in section 3.1.

2.3 Thermometry

Temperature measurement, also known as thermometry, describes the process of measuring a current local temperature. The intuitive concept of a high "temperature" when it is hot and a low "temperature" when it is cold most likely have been around since the concept of numbers were invented. The first ever documented attempt to measure temperature occurred in 170 AD by physician Claudius Galenus [45]. Galenus mixed equal portions of ice and boiling water to create a "neutral" temperature standard. However, the first non crude attempt to measure temperature was in the 1600s by Galileo and other Florentine scientists. They were able to measure relative changes in temperature, but subjected to atmospheric pressure changes. These early devices were called thermoscopes. The first sealed thermometer, which was not subjected to atmospheric fluctuations, was constructed in 1641 by the Grand Duke of Toscani, Ferdinand II [45]. The development of today's thermometers and temperature scales began in the early 18th century, when Gabriel Fahrenheit produced a mercury thermometer and scale. Although these mercury thermometers are close to obsolete, due to the toxicity of mercury.

2.3.1 Gas Thermometers

A thermometer is called a primary thermometer when the measured quantity can be mapped directly to the temperature without introducing any other unknowns. An example of such a thermometer is the gas thermometer.

2.3.2 Thermistors

A thermistor is an element with an electrical resistance that changes in response to temperature. Its name is derived from "thermally sensitive resistor", the original name for these devices. Thermistors were first discovered by Michael Faraday in 1833, although commercially useful thermistors were not manufactured until 1930. Thermistors are typically made from semiconductors in which the semiconductor's resistance drops as a function of temperature, due to excess charge carriers. The resistance to temperature dependence can be characterized with the B parameter equation, which is essentially a simpler form of the Steinhart-Hart equation, where

$$\frac{1}{T} = \frac{1}{T_0} + \frac{1}{B}\ln\left(\frac{R}{R_0}\right), \tag{2.27}$$

or equivalently

$$R = R_0 e^{-B\left(\frac{1}{T_0}-\frac{1}{T}\right)}. \tag{2.28}$$

Where the temperatures are in kelvin, and R_0 is the resistance at temperature T_0. This implies that thermistors are secondary thermometers and would therefore be required to be first calibrated first with a primary thermometer.

Although one could use Ohm's law ($R = \frac{V}{I}$) directly by applying a known voltage and measuring the current across the resistor, this direct approach would require an ammeter

to be connected in series. However, most compact microcontrollers which are used for temperature recordings, have a built-in voltage Digital to analogue converters, and hence the configuration in fig. 2.21 is more often used. In this configuration, a known voltage source, V_x and known resistor, R_1 are connected in series with the thermistor, R_T. Using a simple

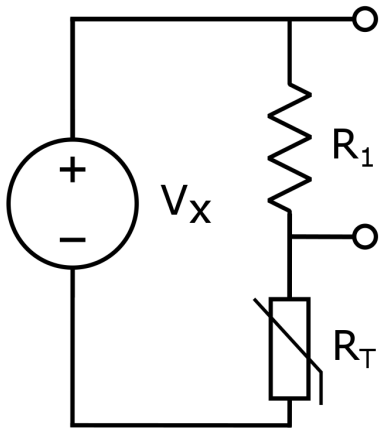

Figure 2.21: Typical configuration for thermistor measurements.

voltage divider equation we have that the voltage drop across R_1 is just:

$$V_{R_1} = V_x \frac{R_1}{R_1 + R_T}, \tag{2.29}$$

hence, by measuring the voltage drop across R_1, the thermistor resistance and in turn the temperature, can also be found.

One of the biggest disadvantages of thermistors is that, according to eq. (2.28), when the temperature gets large enough their resistance saturates to $R_0 e^{-B/T_0}$. Hence, at high enough temperatures, typically 100°C, thermistors can no longer be used.

2.3.3 Silicon bandgap temperature sensor

The silicon bandgap temperature sensor is an extremely common thermometer used in electronic equipment. Its main advantage is that it can be included in a silicon integrated circuit at very low cost. In such a sensor, the forward voltage of a silicon diode, which may be the base-emitter junction of a bipolar junction transistor (BJT), is temperature-dependent, according to the following equation:

$$V_{BE} = V_{G_0}\left(1 - \frac{T}{T_0}\right) + V_{BE_0}\left(\frac{T}{T_0}\right) + \left(\frac{nk_BT}{q}\right)\ln\left(\frac{T_0}{T}\right) + \left(\frac{KT}{q}\right)\ln\left(\frac{I_C}{I_{C_0}}\right), \tag{2.30}$$

where T is the temperature in kelvins, T_0 is some reference temperature, V_{BE0} is the junction voltage at temperature T_0 and current I_{C0}, k_b is the Boltzmann's constant, q is the elementary charge and n a device dependent constant. In theory one could use a primary thermometer

to calibrate for all the unknowns of the BJT's temperature dependencies. However, if we are to compare the voltage of two identical devices at different collector currents,

$$\Delta V_{BE} = \frac{k_B T}{q} \ln\left(\frac{I_{C1}}{I_{C2}}\right). \tag{2.31}$$

We see that most of the variables have been eliminated and we now have a measurable parameter which is directly dependent on absolute temperature, which makes silicon bandgap temperature sensors primary thermometers. The Brokaw bandgap reference configuration shown in fig. 2.22 is typically used.

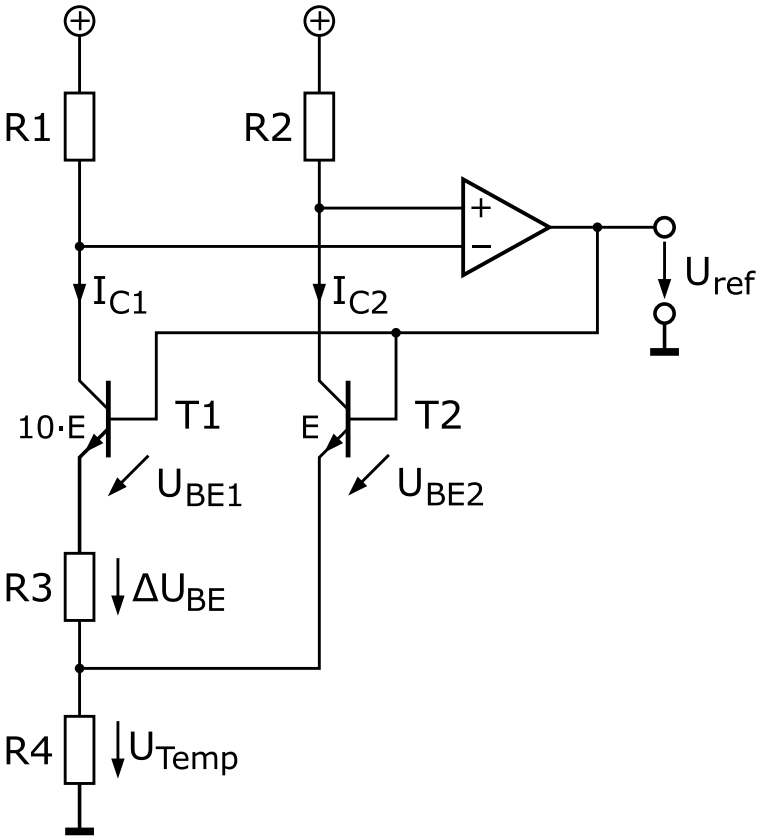

Figure 2.22: Circuit of a Brokaw bandgap reference.

2.3.4 Thermocouples

In 1821, the German physicist Thomas Johann Seebeck discovered that when different metals are joined at the ends and there is a temperature difference between the joints, a magnetic field is observed. At the time Seebeck referred to this as thermo-magnetism. The magnetic field he observed was later shown to be due to thermo-electric current. For practical uses, the voltage generated at a single junction of two different types of wires is what is of interest as this can be used to measure temperature at very high and low temperatures.

There are 8 main types of thermocouples: K, J, N, R, S, B, T, and E, with the difference being the type of metal being used. A standard K-type thermocouple configuration is shown

in fig. 2.23. Under open-circuit conditions where there is no internal current flow, the voltage gradient, ∇V is directly proportional to the temperature gradient ∇T:

$$\nabla V = -S(T)\nabla T. \tag{2.32}$$

where $S(T)$ is a temperature-dependent material property known as the Seebeck coefficient. The standard measurement configuration shown in fig. 2.23, shows four temperature regions and thus four voltage contributions:

1. Change from T_{meter} to T_{ref}, in the lower copper wire.
2. Change from T_{ref} to T_{sense}, in the alumel wire.
3. Change from T_{sense} to T_{ref}, in the chromel wire.
4. Change from T_{ref} to T_{meter}, in the chromel wire.

The first and fourth contributions cancel each other out exactly. As a result T_{meter} has no influence on the measured voltage. The overall measured voltage will be

$$V = \int_{T_{ref}}^{T_{sense}} (S_+(T) - S_-(T))dT, \tag{2.33}$$

where S_+ and S_- are the Seebeck coefficients of the two different types of metals, which for the K-type thermocouple in fig. 2.23, are chromel and alumel.

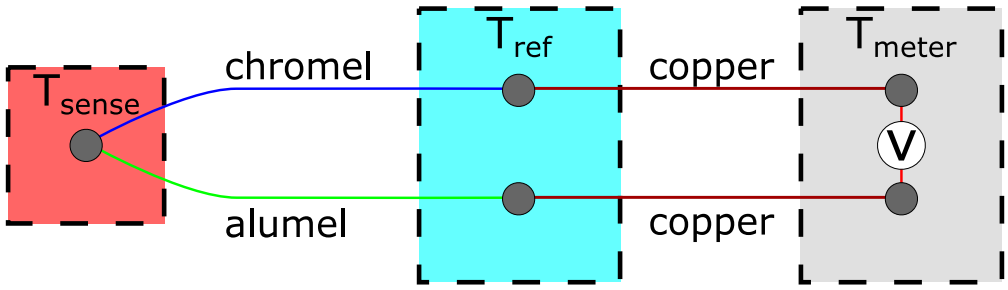

Figure 2.23: K-type thermocouple (chromel-alumel) in the standard thermocouple measurement configuration.

To obtain T_{sense}, it is not sufficient to just measure the voltage, the temperature at the reference junction must also be known. Typically, two strategies are used: the reference junction block is immersed in a semi-frozen bath of distilled water at atmospheric pressure. The precise temperature of the melting point phase transition acts as a natural thermostat, fixing T_{ref} at 0°C. The second strategy is to allow the reference junction to vary in temperature while being monitored with a second thermometer such as a silicon bandgap thermometer.

2.3.5 Infrared Thermometers

Infrared thermometers are the only type of noncontact tempearture that allow for the temperature of an object to be measured from a distance. To understand how infrared thermometers work one need to first understand the concept of black-body radiation.

Black-body radiation is the thermal electromagnetic radiation within or surrounding a body in thermodynamic equilibrium with its environment, or emitted by a body that absorbs all electromagnetic radiation also known as a black body. The thermal radiation spontaneously emitted by many ordinary objects can be approximated as black-body radiation scaled with an emissivity.

Plank's law state that the spectral radiance per unit wavelength is given by:

$$B_\lambda(\lambda, T) = \frac{2hc^2}{\lambda^5} \frac{1}{e^{\frac{hc}{\lambda k_B T}} - 1}. \tag{2.34}$$

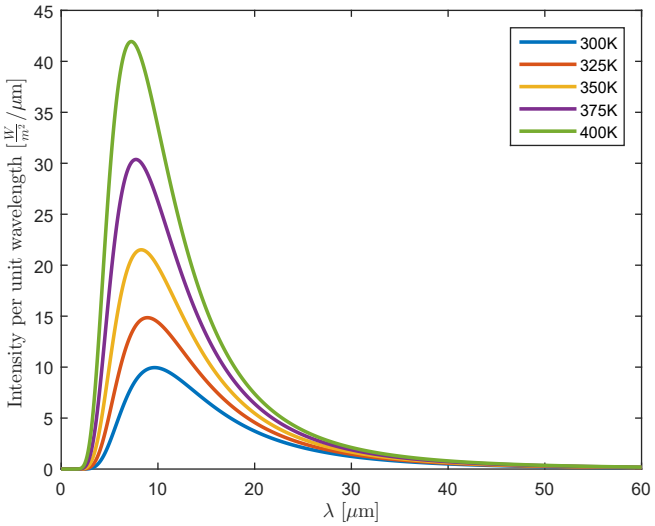

Figure 2.24: Emitted specrum of objects at different temperatures in vacuum.

The spectra for objects from 300K to 400K is shown in fig. 2.24. We see that the peaks of these spectra are in the infrared, which is why an infrared-sensitive material such as Ge or Si is required to measure the emitted radiation of these objects, giving these thermometers the "infrared" name. However, equation eq. (2.34) assumes that the object is placed in a vacuum. Everyday objects also absorbs the radiation from the surrounding. Assuming that the surronding stays at a constant temperature of 300K, the net emission spectra would be that of fig. 2.25. Similar to thermocouples, infrared thermometers require a second thermometer to measure the surrounding temperature.

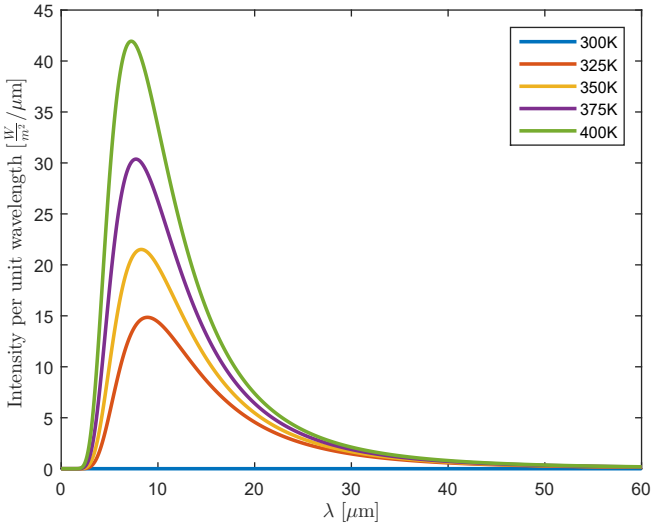

Figure 2.25: Net emitted spectrum of objects at different temperatures in vacuum.

2.4 Control System

2.4.1 Stability

We will only consider linear, time invariant (LTI), and single-input-single-output (SISO) systems. Multi-Input-Multi-Output (MIMO) systems, are systems with more than one input/output. In such cases variables are represented by vectors instead of simple scalar values. Because such a system is linear and time invariant, it can be characterized with a transfer function equation[46],

$$y(t) = \int h(t-\tau)x(\tau)d\tau = h(t) * x(t), \tag{2.35}$$

where $x(t)$, $y(t)$ denote the input and output signal, and $h(t)$ represents the impulse response of the system. Taking the Laplace transform of eq. (2.35) we get

$$Y(s) = H(s)X(s), \tag{2.36}$$

where $Y(S)$, $H(s)$ and $X(s)$ are the Laplace transform of $y(t)$, $h(t)$ and $x(t)$. Although eq. (2.35) and eq. (2.36) are equivalent, eq. (2.36) is more often used as systems connected in series would only require multiplication in Laplace space.

For LTI systems, its stability is commonly defined as bounded input bounded output (BIBO) stable. The system is BIBO stable if $|x(t)| < m_x$ implies $|y(t)| < M_x$, with constants m_x, M_x depending on $x(t)$. Equivalently, an LTI system is BIBO stable if and only if

$$\left| \int_0^\infty h(t)dt \right| < \infty. \tag{2.37}$$

2.4.2 Feedback Control

There are two common classes of control action, open loop control systems, and closed loop control systems. In an open loop control system, the control action from the controller is independent of the process output. In a closed loop control system, the control action from the controller is dependent on the desired and actual process output values. For PCR temperature control, we require closed loop control system. Thus, for the remainder of the thesis we will be discussing closed loop control systems.

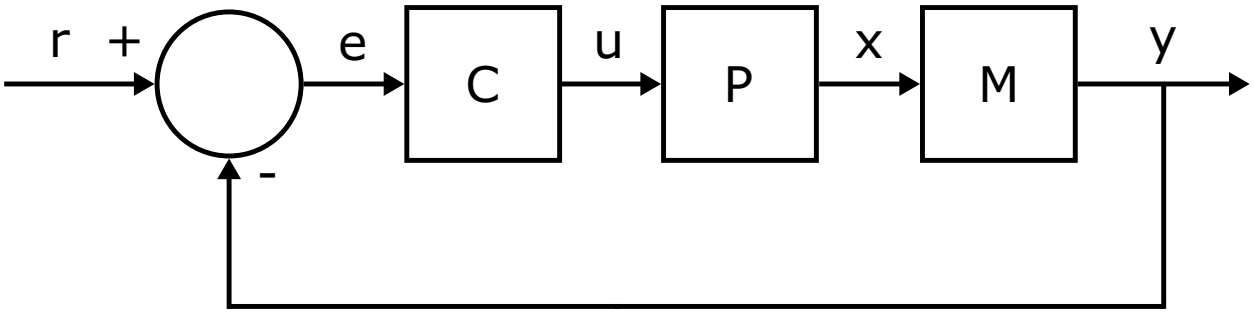

Figure 2.26: Feedback control loop block diagram

The block diagram of all feedback systems can be represented by the block diagram shown in fig. 2.26. The output of the system, $y(t)$, is fed back and compared with the reference value $r(t)$. The controller C then takes the error e or difference between the reference and the output and changes the input u to the system under control P to give x. x is then measured by M to get $y(t)$ to be then fed back again. If we assume the controller C, the process P and the measurement M are LTI, the systems above can be analysed using the Laplace transform on the variables. This gives the following relations:

$$\begin{aligned} Y(s) &= M(s)P(s)U(S) \\ U(s) &= C(s)E(s) \\ E(s) &= R(s) - Y(s). \end{aligned}$$

Solving for $Y(s)$ in terms of $R(s)$ gives

$$\begin{aligned} Y(s) &= \left(\frac{M(s)P(s)C(s)}{1 + M(s)P(s)C(s)} \right) R(s) \\ &= H(s)R(s). \end{aligned} \tag{2.38}$$

$H(s)$ is known as the closed-loop transfer function of the system. The numerator in eq. (2.38) is referred to as the open loop gain of the system. After a quick inspection of eq. (2.38) we find that the only way for a bounded input $R(s)$ to have an unbounded output $Y(s)$ is when $P(s)C(s) = -1$. We will now discuss the different types of controllers that are commonly used.

2.4.3 Controllers

In the proportional control algorithm, the controller output is proportional to the error signal, which is the difference between the setpoint and the process variable. In other words, the output of a proportional controller is the product of the error signal and the proportional gain. This can be mathematically expressed as,

$$u(t) = K_p e(t), \tag{2.39}$$

where K_p is the proportional gain. taking the Laplace transform of both sides we find that the transfer function of proportional controller is

$$C_{prop}(s) = \frac{U(s)}{E(s)} = K_p. \tag{2.40}$$

Integral control is where

$$u(t) = K_I \int_o^t e(\tau) d\tau, \tag{2.41}$$

giving a controller transfer function of

$$C_{int}(s) = \frac{K_I}{s}. \tag{2.42}$$

Derivative control is where

$$u(t) = K_d \frac{de(t)}{dt}, \tag{2.43}$$

giving a controller transfer function of

$$C_{der}(s) = K_d s. \tag{2.44}$$

One of the most widely known controllers is the proportional-integral-derivative controller (PID) which is a combination of the three controllers in which

$$C_{PID}(s) = K_p + \frac{K_I}{s} + K_d s = \frac{K_d s^2 + K_p s + K_I}{s}. \tag{2.45}$$

There are also variations of PID controllers such as PI controllers and PD, where

$$C_{PI}(s) = K_p + \frac{K_I}{s}, \tag{2.46}$$

$$C_{PD}(s) = K_p + K_d s. \tag{2.47}$$

The on-ff or bang-bang control, is the simplest form of feedback control. An on-off controller simply drives the manipulated variable from fully closed to fully open depending on the position of the controlled variable relative to the setpoint. i.e

$$C = \begin{cases} 1 & \text{for} \quad e > 0 \\ 0 & \text{for} \quad e < 0. \end{cases}$$

Although on-off controllers are the easiest to implement, mathematically $C(e)$ is not a linear system, and hence have no $C(s)$.

While on-off controllers have the largest steady state error, they also reach steady-state the quickest. Proportional controllers are mostly used in first order processes with some form of energy storage to stabilize the process, by decreasing the steady state error. As the proportional gain factor K_p increases, the steady-state error of the system decreases. However, despite the reduction, proportional controllers can never manage to eliminate the steady state error of a system [46].

PI controllers are mainly used to eliminate the steady-state error resulting from proportional controller. However, in terms of response time and overall stability of the system, they have a negative impact. The aim of using a PD controller is to increase the stability of the system by improving control since it has the ability to predict the future error of the system response. In order to avoid effects of the sudden change in the value of the error signal, the derivative is taken from the output response of the system variable instead of the error signal [46].

PID controllers may be used in situations where there are excessive delays. The delay can manifest from either the measurement, M, or from the process, P. In these cases lead-lag compensation is required to be effective. The response of the controller can be described in terms of its responsiveness to an error, the degree to which the system overshoots a setpoint, and the degree of any system oscillation [46].

Chapter 3

Experimental Design and Result

3.1 Nanoparticle Inhibition of PCR

One of the drawbacks of PCR is that there is a wide range of chemical and biological substances that would prevent PCR from occurring by interacting with one or more PCR components. However, an inhibition concentration below which PCR would still occur. An example of a PCR inhibitor is SYBR green fluorescent dye, as the intercalation process itself inhibits the PCR. However, SYBR green is still used in QPCR because the inhibition concentration is higher than the concentration of SYBR green required for the fluorescent signal to be measurable.

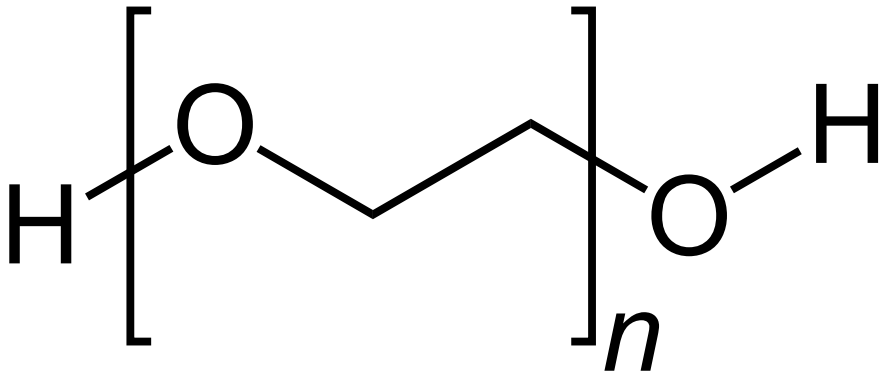

Figure 3.1: Molecular structure of polyethylene glycol

PEGylation is the process of coating the nanoparticles with polyethylene glycol (structure shown in fig. 3.1). Experimentally, for some nanoparticles this coating helps prevent inhibition. We worked with PEG 5000 which means that the n in fig. 3.1 is repeated 5000 times. In our experiment we prepared a typical PCR solution replicating gonorrhea DNA, using both MWCNT and PEGylated MWCNT with different concentrations. The MWCNT have an average length of 1µm and an average radius of 30nm. The solution was then put through thermal cycling with conventional contact PCR. Inspecting the gel electrophoresis results in fig. 3.2, we see that PEGylation does not increase the inhibition concentration of 0.05g/L of MWCNT.

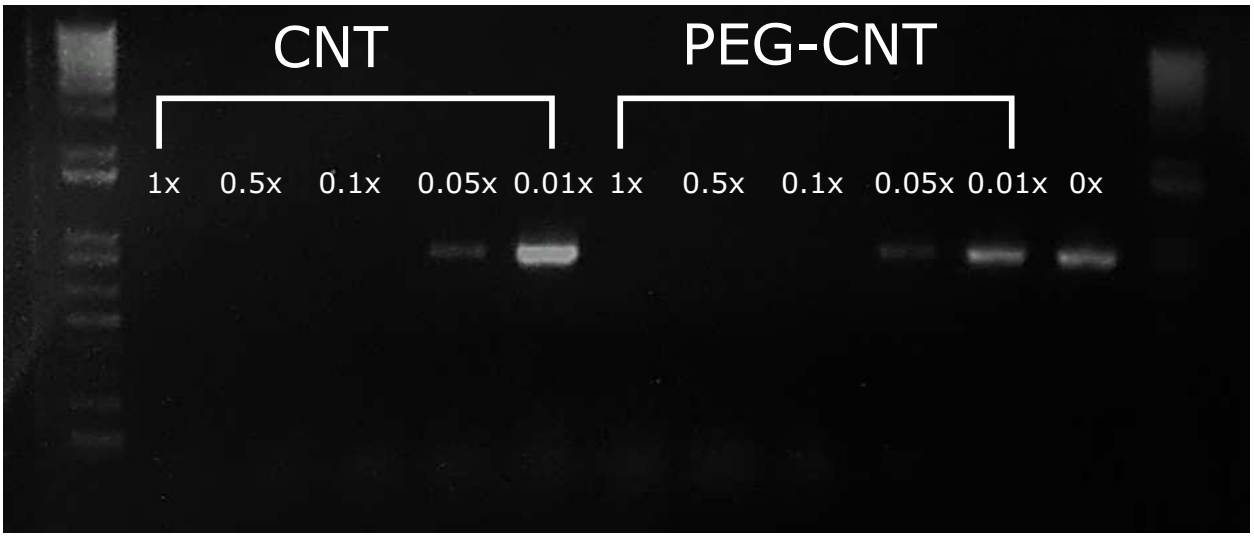

Figure 3.2: Gel electrophoresis for MWCNT and PEGylated MWCNT (1x represents 1g/L, 0.5x represents 0.5g/L and so on).

The same experiment was done for gold nanorods purchased from Nanopartz with a radius of 10nm and an aspect ratio of 4:1. The results for the inhibition concentration are shown in fig. 3.3. We see that the inhibition concentration for uncoated gold nanorods is around 0.5nM.

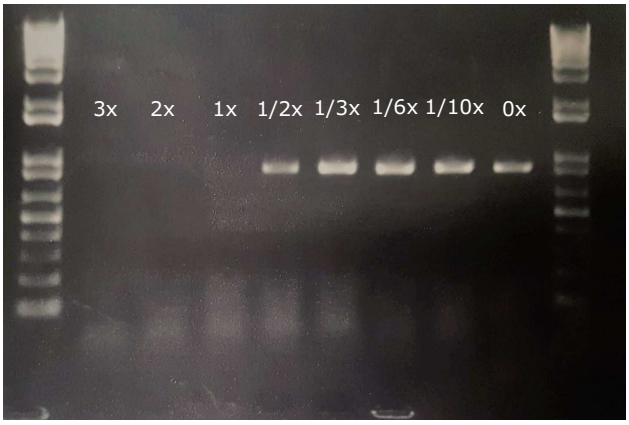

Figure 3.3: Gel electrophoresis for Gold Nanorods (1x respresents 1nM, 1/2x represents 0.5nM and so on).

The results for PEGylated gold nanorods are shown in fig. 3.4. We see that for gold nanorods, the process of PEGylation with PEG 5000 drastically increased the inhibition concentration, to approximately 100nM. We do not yet truly understand the exact interaction mechanism of these nanoparticles which inhibit PCR, or which PCR component(s) interact with the nanoparticles to prevent inhibition. A summary of the inhibition concentration of these nanoparticles is shown in table 3.1. Assuming negligible scattering from nanoparticles,

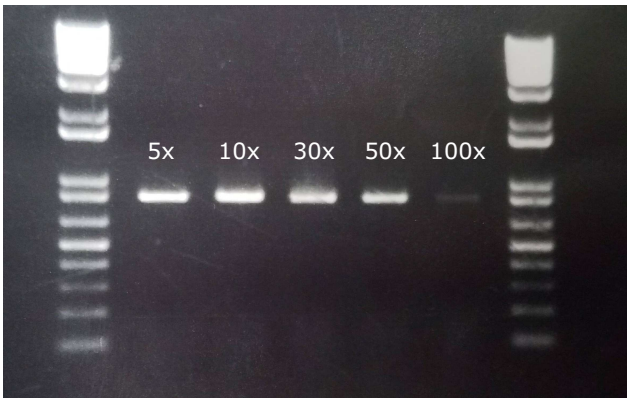

Figure 3.4: Gel electrophoresis for PEGylated Gold Nanorods (5x represents 5nM, 10x represents 10nM and so on).

	CNT	**PEGylated CNT**	**AuNR**	**PEGylated AuNR**
Inhibition Concentration	0.05g/L	0.05g/L	0.5nM	100nM

Table 3.1: Summary of inhibition concentrations for CNT and gold nanorods.

eq. (3.3) gives us the ratio of heating rate to be

$$\frac{R_1}{R_2} = \frac{1 - 10^{A_1 c_1 l}}{1 - 10^{A_2 c_2 l}}. \tag{3.1}$$

Where R_1, A_1, c_1 are the heating rate, absorbance per unit length concentration, and concentration of gold nanorods. R_2, A_2, c_2 are the heating rate, absorbance per unit length concentration, and concentration of MWCNT. Using eq. (3.1) A_2 is approximated to be $1.463 \frac{1}{\frac{g}{L}\mathrm{m}}$. We can thus find the maximum absorbance per unit length for both the MWCNT and gold nanorods before PCR inhibition.

$$\text{Maximum OD per unit length for MWCNT} = 0.0446 \frac{1}{\text{mm}}$$

$$\text{Maximum OD per unit length for Gold Nanorods} = 3.05 \frac{1}{\text{mm}}$$

We thus conclude that PEGylaged nanorods can have an absorbance per unit length 68 times higher than both PEGylated and non-PEGylated MWCNT.

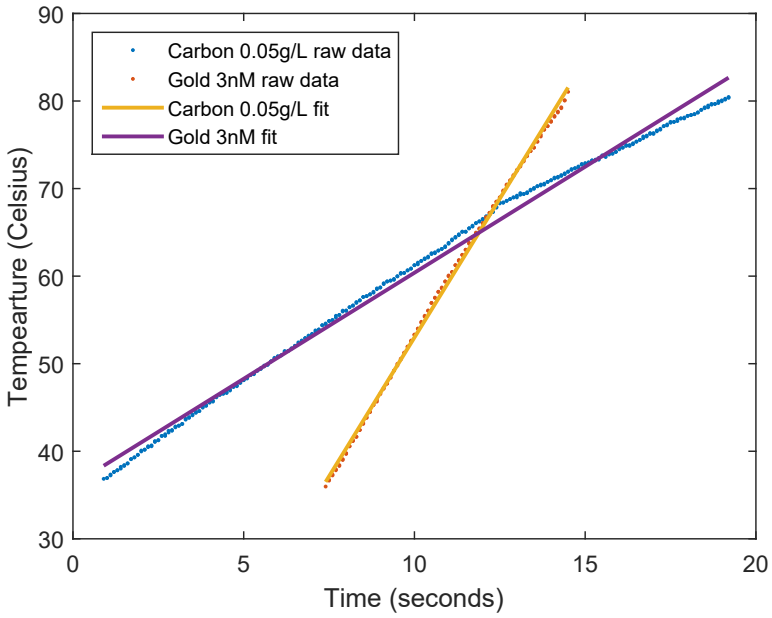

Figure 3.5: Heating curve of gold nanorods and MWCNT.

3.2 System Justifications

We require a system which performs PCR with four main key characteristics; **energy efficient**, **fast**, **compact**, **no down-time**.

3.2.1 Heat Generation Mechanism

Traditional contact heating elements are simple and cheap but at the same time slow and inefficient. The heating element in addition to the PCR tube and reagent would have to be heated. Because heat is transfered through convection and conduction, heat loss due to coupling is the other drawback of contact heating. For non-contact heating, we require a source that is spatially coherent enough to couple effectively into our PCR reagents: this requirement could be fulfilled with a laser. To generate heat with a laser, we could either use a laser in the mid-infrared range or add nanoparticles to our PCR mixture and use a laser close to the visible spectrum. We decided upon the latter and used a laser at 808nm, and gold nanorods, as they are widely available. Using nanoparticles also provides us with the option of tuning the absorption.

The amount of power absorbed from the laser is typically

$$P_{abs} = P_{laser}\frac{\sigma_{abs}}{\sigma_{abs}+\sigma_{scattering}}(1-e^{-(\sigma_{abs}+\sigma_{scattering})Nl}), \tag{3.2}$$

where N is the particle concentration, and l the optical path length which would also be the inner diameter of our tube. For a fixed path length, we would like the concentration to be high enough such that most of the power is absorbed. However, if the concentration becomes much larger relative to the path length, we would get non-uniform heat distribution, which

would be detrimental for PCR. In fig. 3.6, for a fixed path length of 10mm, approximately 100 percent of the light absorbed for both the lower concentration blue curve (absorption per unit length of $0.5\frac{1}{\text{mm}}$) and the higher concentration, orange curve (absorption per unit length of $6\frac{1}{\text{mm}}$). We however see almost all the light is absorbed in the the 1/10 the length of the tube, giving us terrible heat distribution.

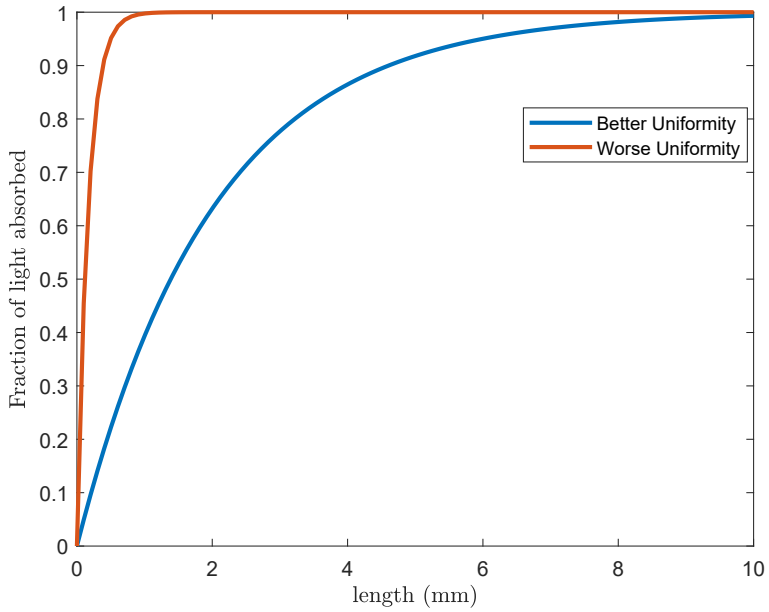

Figure 3.6: Fraction of light absorbed as a function of length.

Using nanoparticles would allow us to always find the optimal concentration for a certain optical path length. This would not be possible to do relying on water absorption in the infrared or microwave spectrum, as the absorption per unit length is fixed and cannot be tuned.

From eq. (2.12) and eq. (2.12), the mass and in turn the volume is to first order approximation inversely proportional to the heating rate. It would be to our advantage to use the smallest volume possible. However, pipetting becomes a challenge as volumes get smaller. We decided on 20µL as the optimal volume before any challenge in pipetting occurs. This corresponds to about 20mg of water. The PCR mixture is contained in a standard Eppendorf polypropylene PCR tube.

3.2.2 Thermometer

Small contact thermometers such as thermocouples or thermistors will have the highest temperature reading accuracy as they are physically in contact with the solution. This however would mean that the PCR machines will have significant downtime, as after each PCR run, the thermometer would have to be cleaned thoroughly to prevent cross contamination. This fact alone dictates that we would have to use an infrared thermometer. The trade-off with infrared thermometers is that although thermal coupling between a liquid and a solid

is quite high, the measured temperature will always be that of the tube but not of the solution itself. However, this may not be a significant problem, as the margin of error for PCR temperature is already rather large. Our infrared thermometer is calibrated with a heating block and thermocouple.

3.2.3 Cooling

Although this system can be cooled passively as all the temperature steps for PCR are higher than typical room temperatures, a PC-blower fan is cheap, simple and drastically increases the cooling rate.

3.2.4 Real-Time Monitoring

As a diagnostic device, real-time monitoring of DNA product is the other key aspect of the system. Although nucleic acid stain such as SYBR green and PICO green can be used, these nucleic acid stain suffers from photobleaching, wherein they permanently lose their ability to emit light even when excited at the correct wavelength [47]. This is further amplified in our system as they are constantly being exposed to a heating laser.

For the reasons listed above we believe that the simplest and most effective method is to measure the transmission of a 260nm, 1mW UV LED. One might ask the question "If this 260nm transmission is so easy and effective, why isn't anyone using them ?". The reason lies in the traditional contact heating mechanism: all contact heating requires a heat spreader like that of fig. 2.14. For the heat spreader to maximize its efficiency it would have to wrap over the entire tube. This however leaves only the top facet left to be accessed. One would need two facets in the same dimension to measure UV transmission. This is the other advantage of direct non-contact heating. The diagram of our final system is shown in fig. 3.7 and the picture of our system is shown in fig. 3.8.

	Manufacturer	**Model Number**
Heating Laser	Laserglow	D8050BXSX
Infrared Thermometer	Optris	CS LT
Cooling Fan	Sanyo Denki	9BMB12P2K01
UV LED	Thorlabs	LED260J
UV Photodetector	Thorlabs	PDA25K

Table 3.2: Summary of system's components.

3.2.5 Control System

As being able to reach different temperature quickly for different steps of a PCR cycle is the most important factor, on-off control should be implemented. The disadvantage comes in the form of oscillation in steady-state. The larger the delay in the response time of the system, the larger this oscillation will be. This effect is shown in fig. 3.9, by applying finite time difference approximation to eq. (2.11) in conjunction with the on-off control algorithm.

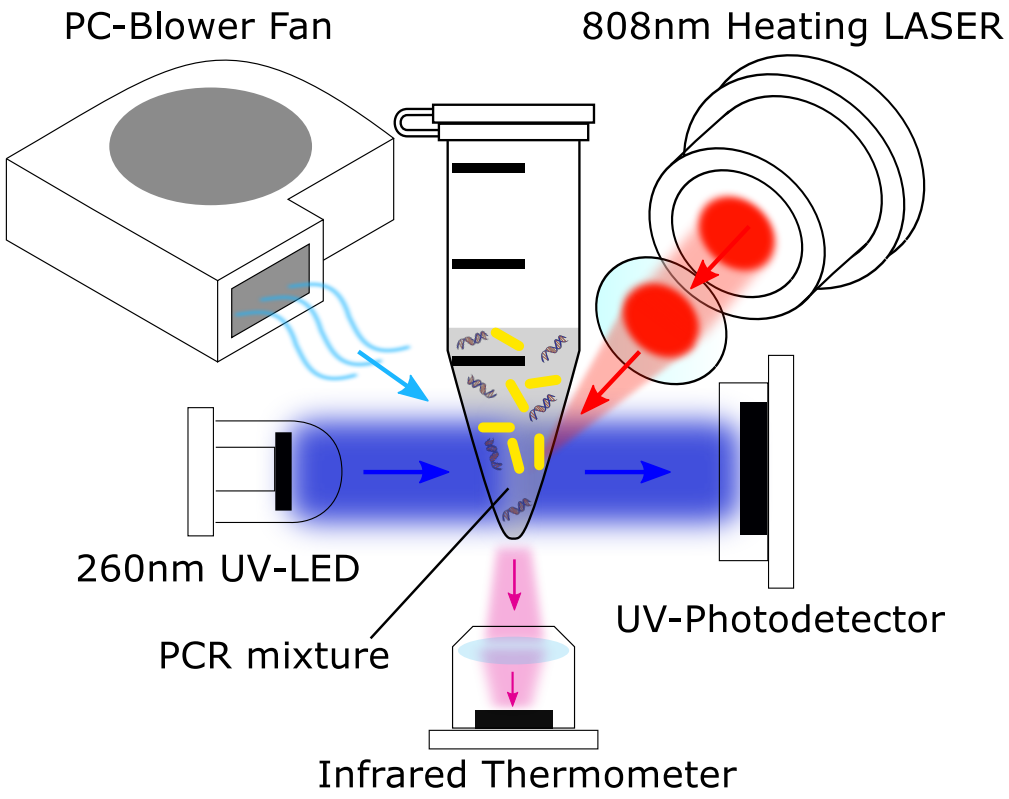

Figure 3.7: Diagram of final system.

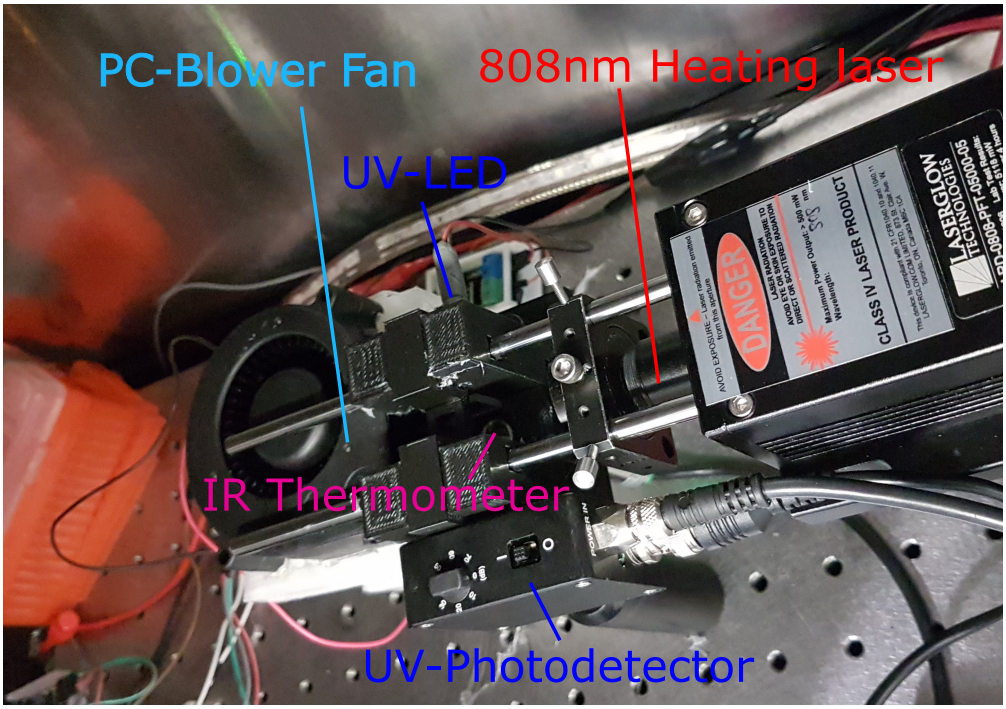

Figure 3.8: Picture of final system.

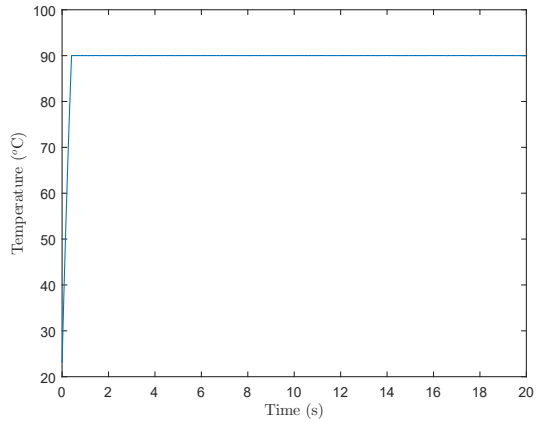

(a) No delay

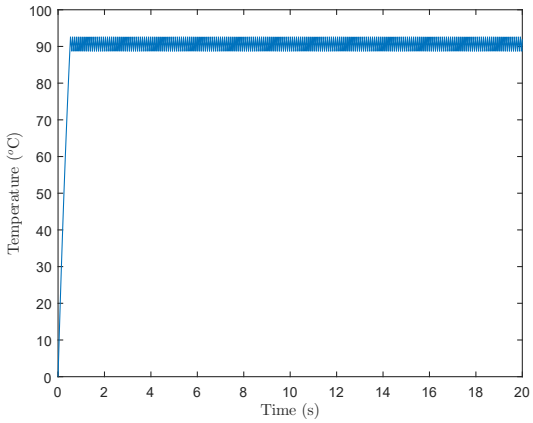

(b) 200ms delay

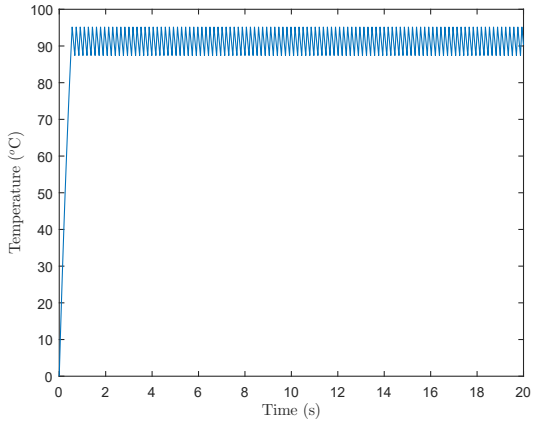

(c) 400ms delay

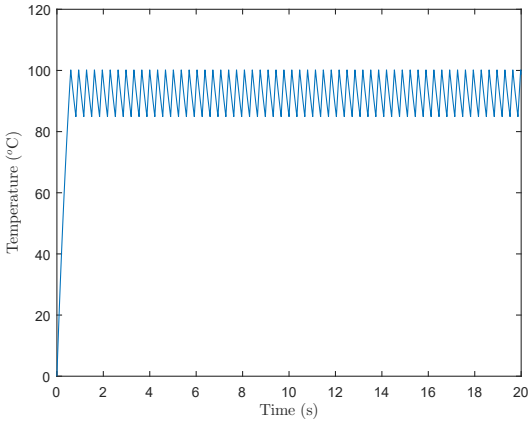

(d) 800ms delay

Figure 3.9: Effect of delay on on-off control systems, plotted for for temperature as a function of time.

As mentioned before, proportional control is often introduced to dampen the oscillatory behaviour of the system at equilibrium. Our heating system cannot truly have proportional control, as the cooling rate is always fixed and cannot be controlled, additionally the output power is clamped at the maximum power of the laser. The control parameter that is fed into the laser takes the form:

$$C = \begin{cases} \frac{e(t)}{K} \quad (1 \quad \text{for} \quad C > 1) \quad \text{for} \quad e > 0 \\ 0 \quad \text{for} \quad e < 0. \end{cases}$$

In fig. 3.10, we see that although large K parameters can dampen out the oscillation even when the delay in our system is large, this causes the equilibrium temperature to be lower than the actual target temperature of 90°C (see fig. 3.10). Experimentally we find that the delay is small enough to keep the oscillation of on-off control within 1°C of the target temperature. Due to the downside associated with proportional control, we believe that the simple on-off control is most effective for fast PCR.

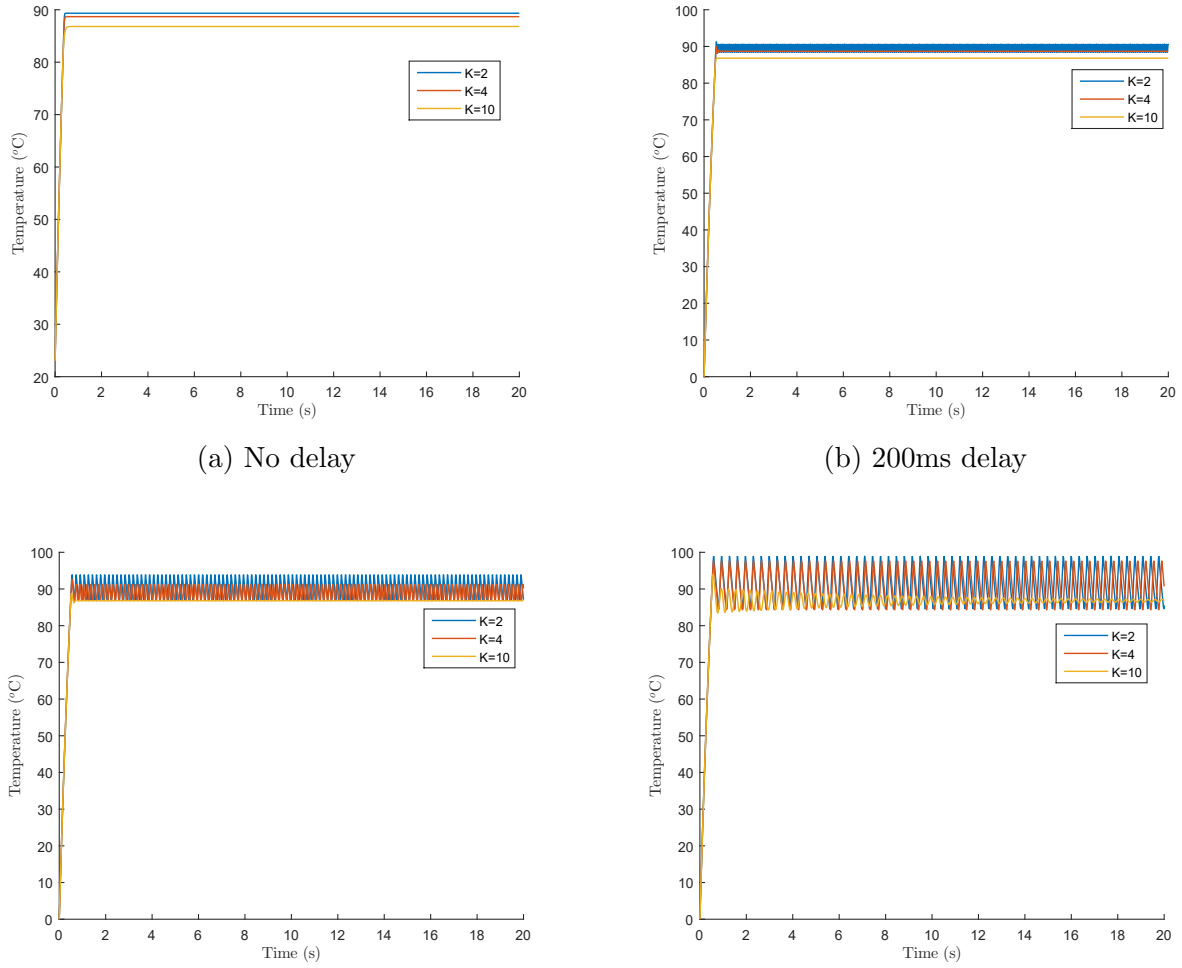

(a) No delay

(b) 200ms delay

(c) 400ms delay

(d) 800ms delay

Figure 3.10: Effect of delay on proportional control systems, plotted for for temperature as a function of time.

3.3 Heating Data

The 500µL PCR tubes filled up to 20µL have an average inner diameter of about 3mm, taking this as our optical path length and using eq. (2.7), we predict that about 82% of the light will be absorbed. The heating curve of our PCR cycle is shown in fig. 3.11. The temperature was held at each stage for 5 seconds. The basic temperature statistics at each holding stage are summarized in table 3.3.

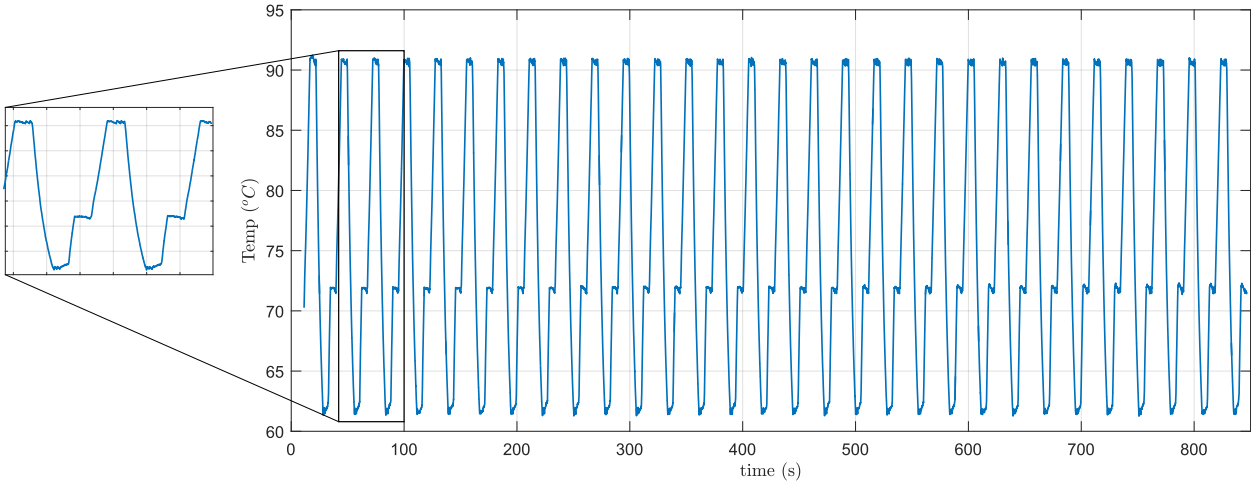

Figure 3.11: System heating curve for 35 PCR cycles.

	Denaturation	**Annealing**	**Elongation**
Target Temperature	90.5°C	61.5°C	71.5°C
Average Temperature	90.7°C	61.8°C	71.6°C
Temperature Fluctuation	±0.34°C	±0.55°C	±0.28°C

Table 3.3: Temperature statistics at each PCR stage.

Because our input power is very large, eq. (2.12) can be linearly approximated to,

$$T(t) = T_o + \frac{P_{in}(1 - e^{-\mu cl})}{m_w c_w} t. \tag{3.3}$$

It can be clearly seen from fig. 3.11 and fig. 3.12 that even at the highest temperature range (72°C to 91°C), our linear approximation is still valid. With 2W of power coming from the laser heating 25mg, eq. (3.3) predicts that the heating rate should be $19.09\frac{^\circ C}{s}$, which is much higher than our experimental heating rate of $6.12\frac{^\circ C}{s}$. This is most likely due to the mass of the polypropylene PCR tube not being included in our calculations, as it is the temperature of the tube that is being measured. If we are to take the mass of polypropylene into account, we would have to change $m_w c_w$ to

$$m_{eff} c_w = m_w c_w + m_{pp} c_{pp}. \tag{3.4}$$

Where $m_p p$, c_{pp} are the mass of polypropylene and heat capacity of polypropylene respectively. Hence, with the polypropylene tube our effective water mass becomes m_{eff}=78mg.

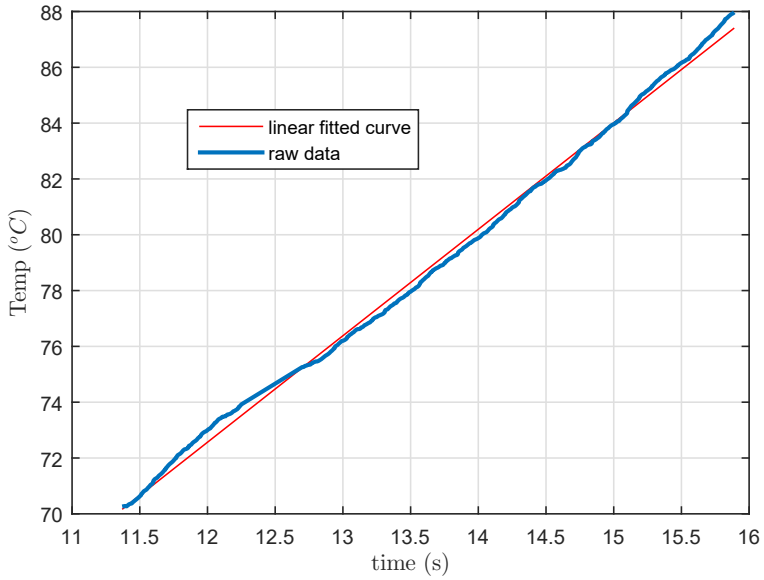

Figure 3.12: Validty of Linear Approximation.

3.4 PCR Optimization

3.4.1 PCR Temperatures

We would now like to know what the temperature range and the efficiency are in this range for temperatures at each stage. fig. 3.13 and fig. 3.14 show the electrophoresis gel image with varying denaturing temperatures for plasmonic PCR. The temperature was held

for 5 seconds at each PCR stage of denaturing at varying temperatures, annealing at 55°C, and elongating at 72°C for 30 cycles, with as starting DNA concentration of 10^4 Chlamydia Trachomatis (CT) DNA copies per 20µl. We see that the PCR is most efficient at 87°C for the denaturing stage. This is because not enough template DNAs denature at low denaturing temperatures, while denaturing temperatures too high will permanently damage the polymerase.

Figure 3.13: Gel electrophoresis with varying denaturing temperatures from 79°C to 90°C.

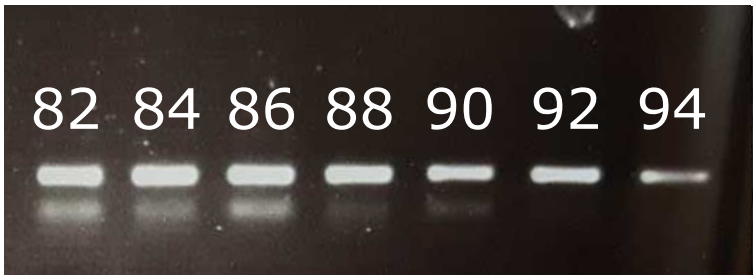

Figure 3.14: Gel electrophoresis with varying denaturing tempearatures from 82°C to 94°C.

We then varied the annealing temperature while keeping the denaturing stage at 87°C and elongating stage at 72°C for 30 cycles. All stages were held for 5 seconds and the resulting electrophoresis gel image is shown in fig. 3.15a and fig. 3.15b.

We observe that the optimal annealing temperature is at 62°C. Lower temperature leads to nonspecific binding, whilst higher temperature will prevent efficient binding of the primers.

3.4.2 Limit of Detection

What is the mininum starting DNA concetration which will allow us to confirm PCR has occured? Of course, the answer to this question would depend on what the exact detectiod method is. We will first explore the detection limit for the semi-quantitative method of ethidium bromide gel electrophoresis. We varied the starting DNA concentration while keeping the optimal PCR temperatures from section 3.4.1, holding for 5 seconds at each stage for 30 cycles. We see that our limit of detection for ethidium bromide is at 10^3 DNA copies per 20µL.

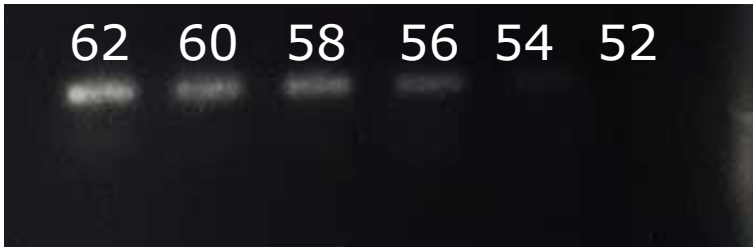

(a) Annealing temperature varied from 52°C to 62°C.

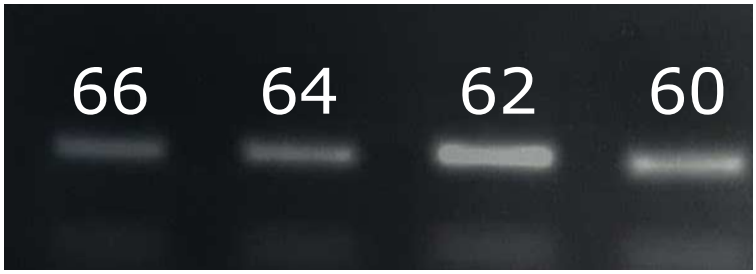

(b) Annealing temperature varied from 60°C to 66°C.

Figure 3.15: Gel electrophoresis with varying annealing tempearatures.

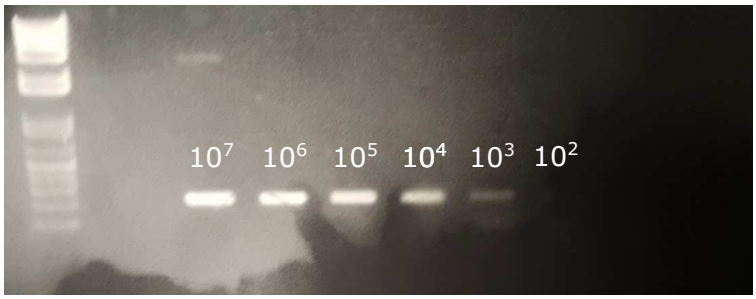

Figure 3.16: Gel electrophoresis with varying starting DNA concentrations, each number represents the copies of DNA per 20µl i.e. 10^n represents 10^n DNA copies per 20µL.

Figure 3.17: Gel electrophoresis with varying hold time at optimal PCR temperatures. $n_1n_2n_3$ represent holding for n_1 seconds at denaturing, n_2 seconds at annealing and n_3 seconds at elongation (e.g. 555 means 5 seconds for denaturating, 5 seconds for annealing and 5 seconds for elongation).

3.4.3 Hold Time Limit

As having a fast reaction is an important criterion, we want to see if there are any other parameters we can change to have a PCR product in a shorter time. We investigated this by changing the hold time at each PCR stage; the results are shown in fig. 3.17. We see that we can reduce the hold time to 1 second for both elongating and denaturing stage. However, we have no visible PCR product when the annealing temperature is reduced to 1 second.

We varied the annealing temperatures from 60°C to 62°C and annealing time. In the gel electrophoresis results shown in fig. 3.18, we see that we could further reduce the hold time by having a lower annealing temperature. At 60°C we could reduce the hold time to 2 seconds. Although the band is very faint, PCR technically did occur even with a hold time of 1 second when the annealing temperature is at 60°C. Increasing the annealing temperature to 64°C requires a longer hold time, as the band is already very faint at a hold time of 3 seconds. The results are in strong agreement with the experimental and theoretical data

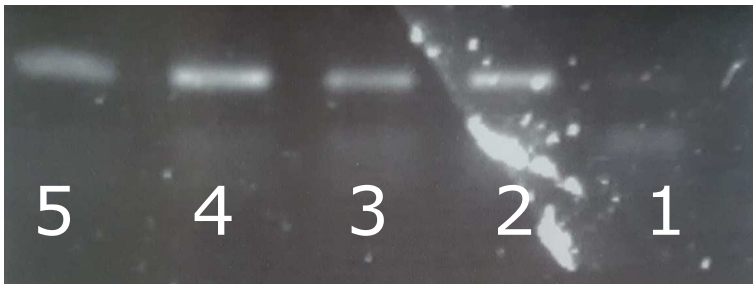

(a) Annealing time variation with temperature kept at 60°C.

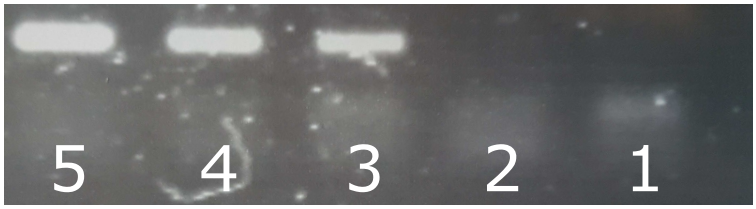

(b) Annealing time variation with temperature kept at 62°C.

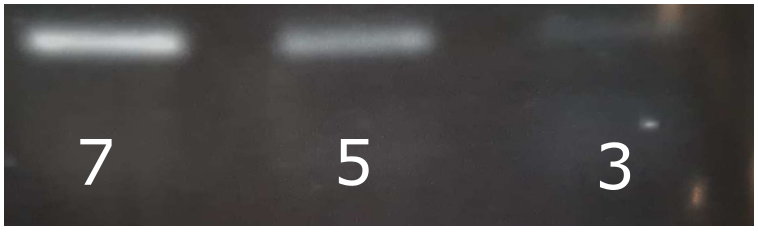

(c) Annealing time variation with temperature kept at 64°C.

Figure 3.18: Gel electrophoresis with varying annealing temperatures.

from Mamedov [18]. If one wishes for maximum PCR efficiency, the hold time would have to be longer for higher annealing temperatures.

The total PCR hold time follows the simple formula:

$$t_{TotalPCR} = cycles \times (t_{hold_{anneal}} + t_{hold_{elongate}} + t_{hold_{denature}} + (H_R + C_R)(T_{denature} - T_{annealing})) \tag{3.5}$$

where $t_{hold_{anneal}}$, $t_{hold_{elongate}}$ and $t_{hold_{denature}}$ are the annealing hold time, elongation hold time and denaturing hold time, respectively. H_R, C_R, $T_{denature}$ and $T_{annealing}$ are the average cooling rate, average heating rate, denaturing temperature, and annealing temperature. To optimize the PCR time and PCR efficiency for our system we would want the annealing temperature to be around 62°C with a hold time of 3-4 seconds.

3.4.4 Beam Size

We varied the beam size to see what effect this would have on our PCR product. As the total energy absorbed by the PCR mixture is regardless of beam size, we achieved the same heating rate and total PCR time. The beams were varied from a large beam that covers the entire PCR tube, shown in fig. 3.21, to a medium-sized beam that covers approximately 70 percent of it, shown in fig. 3.20 and then finally focused to the smallest possible beam size for the gaussian beam, shown in fig. 3.19. The PCR was performed with the optimized parameters with gel electrophoresis results shown in fig. 3.22 and the second experiment with only a small beam and large beam shown in fig. 3.23. We see that if the beam is too small we get very poor PCR efficiency. This is most likely due to bad heat distribution when the beam is focused. Thus, we would want the beam size to be as large as possible while keeping all of the beam inside the tube.

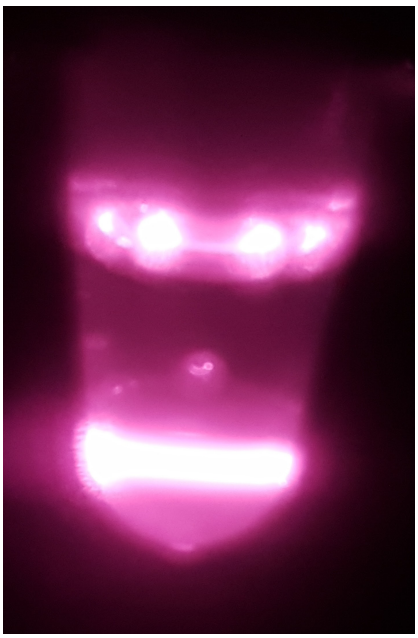

Figure 3.19: Small beam.

Figure 3.20: Medium beam.

Figure 3.21: Large beam.

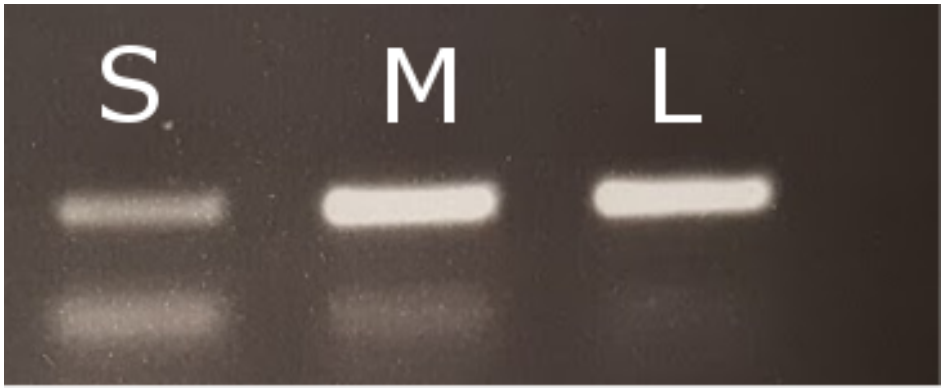

Figure 3.22: Gel electrophoresis with varying beam size, S is a small sized beam, M is a medium sized beam, and L is large sized beam.

Figure 3.23: Gel electrophoresis with varying beam size, S is a small sized beam and L is large sized beam.

3.4.5 Contact Heating vs Non-Contact Heating Efficiency

Now that the system have been optimized, we want to see how its PCR efficiency compares to that of the conventional PCR machines which use contact heating (Eppendorf Mastercycler Nexus Thermal Cycler). The gel electrophoresis results are shown in fig. 3.24. We see that the efficiency is practically the same for all starting DNA concentrations. For the same hold time at all temperatures, our plasmonic system took around 7 minutes, while the conventional PCR took 39 minutes.

3.5 Real Time Detection

As shown in fig. 3.7, we are measuring the change in transmission at 260nm as free nucleotides are being turned into dsDNA. Using Beer-Lambert's law, the power measured by a photodetector after the UV-light has has traveled through the medium before PCR has occurred follows the formula:

$$P_{measured_{pre}} = (1 - \gamma_L) P_{in} e^{-\mu_{dntp} c_{dntp} l} + \eta_1 \tag{3.6}$$

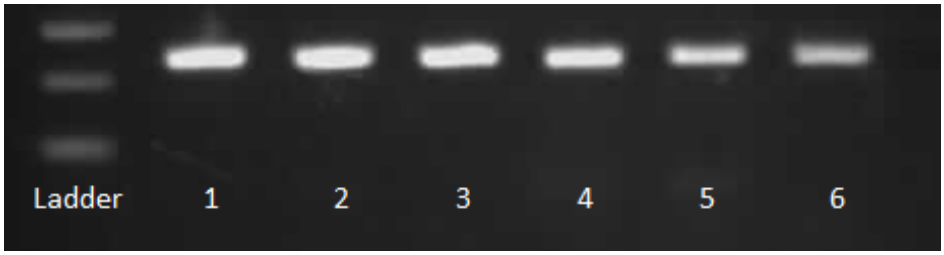

Figure 3.24: Gel electrophoresis of contact gold nanorods PCR vs conventional PCR, Lane 1 is Plasmonic PCR, 10^4 per 20µL CT DNA copies. Lane 2 is Conventional PCR with 10^4 per 20µL CT DNA copies, with AuNR. Lane 3 is Conventional PCR, 10^4 per 20µL CT DNA copies, w/o AuNR. Lane 4 is Plasmonic PCR, 10^3 per 20µL CT DNA copies. Lane 5 is Conventional PCR, 10^3 per 20µL CT DNA copies, with AuNR. Lane 6 is Conventional PCR, 10^3 per 20µL CT DNA copies, w/o AuNR.

where $P_{measured_{pre}}$ is the measured power prior to PCR, γ_L is the loss factor, P_{in} is the input power, μ_{dntp} is the extinction coefficient, c_{dntp} is the starting concentration of dNTP, l is the optical path length and $\eta 1$ is the noise from detection in the pre PCR measurement of our system. After PCR has been completed, the measured power would be

$$P_{measured_{post}} = (1-\gamma_L)P_{in}e^{-(F\mu_{dsdna}c_{dntp}+(1-F)\mu_{dntp}c_{dntp})l} + \eta_2 \tag{3.7}$$

where F is the fraction of dNTP that has turned into DNA, and η_2 is the noise from detection post PCR. Dividing eq. (3.7) by eq. (3.6), and under the assumption of no noise being present in our system we would have the relative intensity to be

$$P_{rel} = e^{Fc_{dntp}(\mu_{dntp}-\mu_{dsdna})l}, \tag{3.8}$$

we can thus track the fraction of dNTP that has been converted to dsDNA by inspecting the relative intensity. However, taking noise from the detection side into account the relative intensity becomes

$$P_{rel_{noisy}} = \frac{1}{\frac{1}{P_{rel}} + \frac{\eta_2 e^{(F\mu_{dsdna}c_{dntp}+(1-F)\mu_{dntp}c_{dntp})l}}{(1-\gamma_L)P_{in}}} + \frac{\eta_1 e^{\mu_{dntp}c_{dntp}l}}{(1-\gamma_L)P_{in}} + \frac{\eta_2}{\eta_1}. \tag{3.9}$$

The first term in eq. (3.9), contains our noiseless relative power mixed with noise pre PCR. The effect of noise pre and post PCR can be minimized by maximizing P_{in} and having the loss factor, γ_L as small as possible.

To get the largest relative change in intensity, $P_{rel_{noisless}}$, we need to get as much dNTP to convert to dsDNA as possible, i.e. getting F as close as possible to unity. We can achieve this by reducing the starting concentration of dNTP. However, reducing the dNTP concentration beyond a certain threshold will decrease PCR efficiency. By varying the starting concentration of dNTP, we experimentally determined the extent to which dNTP concentration can be reduced without hindering our PCR's efficiency. The gel electrophresis result of this is shown in fig. 3.25. We see that reduction in PCR efficiency starts to occur at concentrations lower than 62.5µM. We shall be using this dNTP concentration for our experiments.

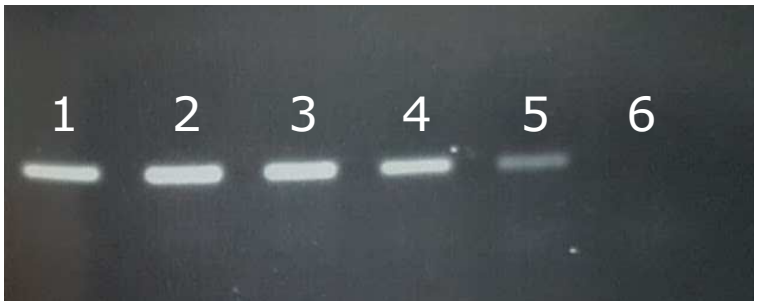

Figure 3.25: Gel electrophoresis with varying dNTP concentration; dNTP concentration of lane 1 is standard 250µM, lane 2 is 125µM, lane 3 is 62.5µM, lane 4 is 31.25µM, lane 5 is 15.625µM, and lane 6 is with standard 250µM and no DNA.

To varify the phenonmenon summarized in table 2.1, we took the spectroscopy of the dNTP dilutions prior to PCR and post PCR; the results are shown in fig. 3.26. We see that because PCR has occured in the first 5 lanes, there is a significant change in absorption in fig. 3.26.

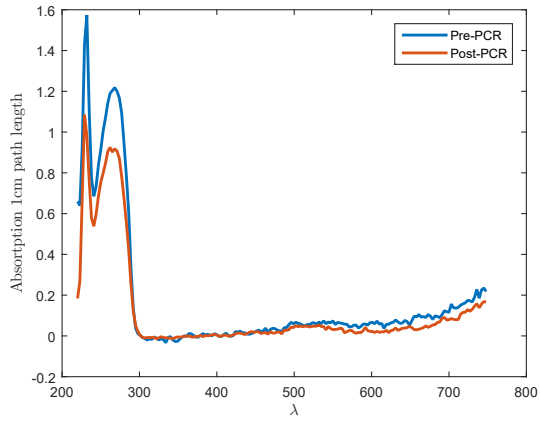

(a) Standard dNTP concentration of 250µM

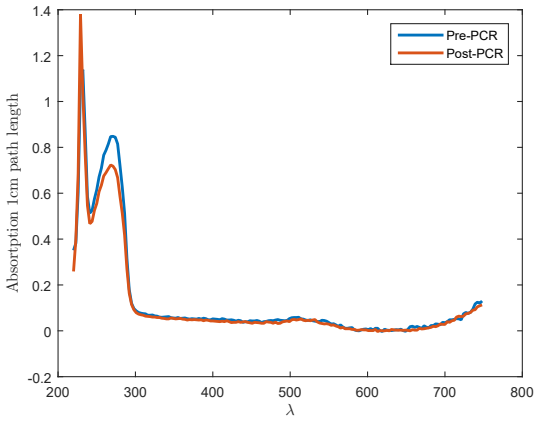

(b) dNTP concentration of 125µM

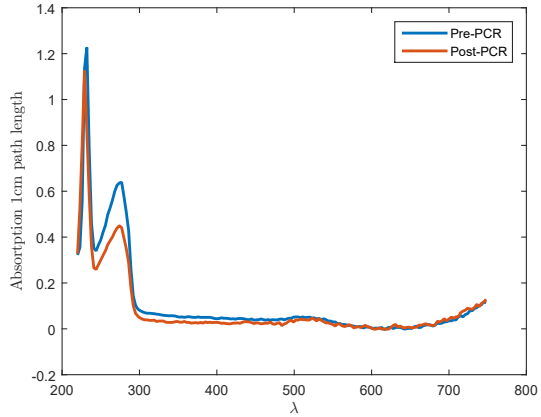

(c) dNTP concentration of 62.5µM

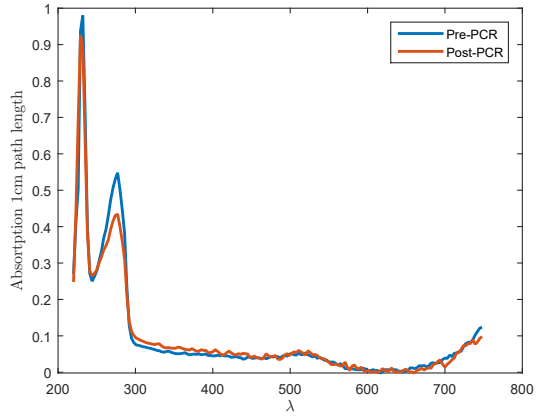

(d) dNTP concentration of 31.25µM

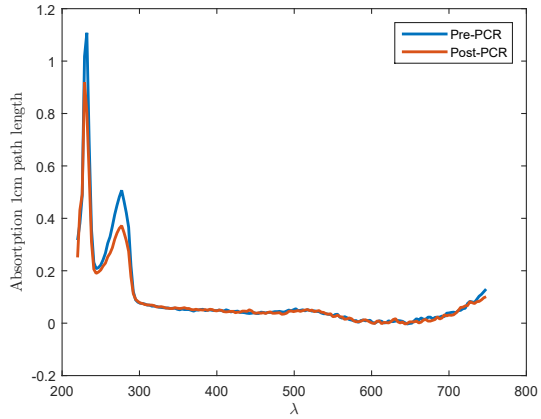

(e) dNTP concentration of 15.625µM

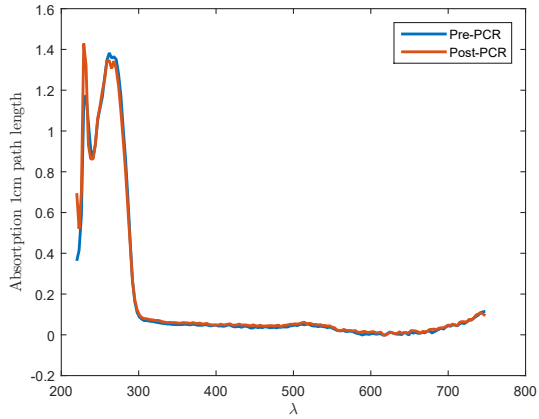

(f) Standard dNTP concentration, no DNA

Figure 3.26: Spectroscopy of vasrying dNTP concentrations.

3.5.1 UV-LED Drawbacks

As metioned at the end of section 2.1.5, prolonged exposure of DNA to UV light can damage it enough that the formation of dsDNA is prevented, and thus no primer binding will occur with the damaged DNA. We wish to know with the optical power of 0.5mW that we are using, how long can we expose the solution to UV light without it hindering PCR. We exponentially varied the exposure time from 0s to 320s, before PCR and after PCR with the gel electophoresis results shown in fig. 3.27 and fig. 3.28. We see that for both pre and post PCR UV exposure, an exposure time greater than 80s will decrease the PCR yield. Assuming that we would need to measure the transmission once every 35 cycles, this tells us that the exposure time per cycle must not exceed $80s/35 \approx 2.29s$.

Figure 3.27: Gel electrophoresis with varying exposure time, pre-PCR of 260nm UV-LED 0.5mW for 0s, 5s, 10s, 20s, 40s, 80s, 160s, 320s.

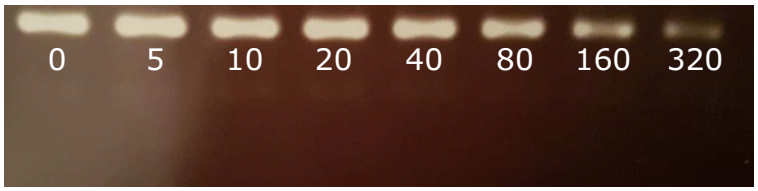

Figure 3.28: Gel electrophoresis with varying exposure time, post-PCR of 260nm UV-LED 0.5mW for 0s, 5s, 10s, 20s, 40s, 80s, 160s, 320s.

3.5.2 Real Time Results

We conducted real-time monitoring with a dNTP concentration of 62.5µM. The UV-LED is turned on for 30ms at each cycle. The relative intensity for both a negative PCR with no template DNA and positve full PCR mix with different starting DNA concentration is shown in fig. 3.30. Depending on the starting DNA concentration, the change in relative intensity reduces very slightly for a number of cycles at the beginning. This could be due to water evaporation in the solution, which causes an increase in concentration and thus, absorption. The more starting DNA conentration is present in our PCR mix, the earlier the change from dNTP to dsDNA reaches a detectable level and we see an exponential increase in relative intensity. For example, we start seeing a positive change in power measured at 16 cycles for 10^6 copies per 20µL.

Once all the primers in our solution has either been extended to dsDNA or turned into primer dimers, further thermal cycling does not change the measured power. The point of saturation will appear earlier for higher starting DNA concentration. In fact, our plot of relative intensity is very similar to the fluorescent curves found in QPCR (fig. 2.10). The gel electrophoresis results shown in fig. 3.29 further assure us of our UV measurement results.

At a DNA template concentration of 10^3 copies per 20µL and lower, the changes in relative intensity are very similar. We hypothesize that, this is due to most of the primers forming primer-dimers instead of extending into the template DNA. This hypothesis is confirmed after inspecting the intensity of the primer-dimer bands bellow our DNA product band in fig. 3.29 of concentrations 10^3 copies per 20µL and less. With the results, our current limit of detection is around 10^4 copies per 20µL. Using eq. (3.8), the estimated fraction of dNTP that has been converted to DNA, with different starting DNA concentrations is summarized in table 3.4.

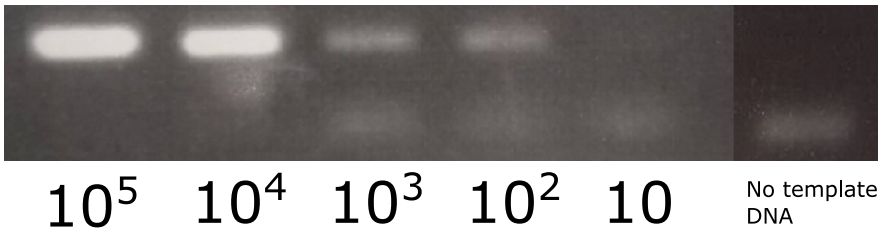

Figure 3.29: Gel electrophoresis confirmation of UV measured PCR.

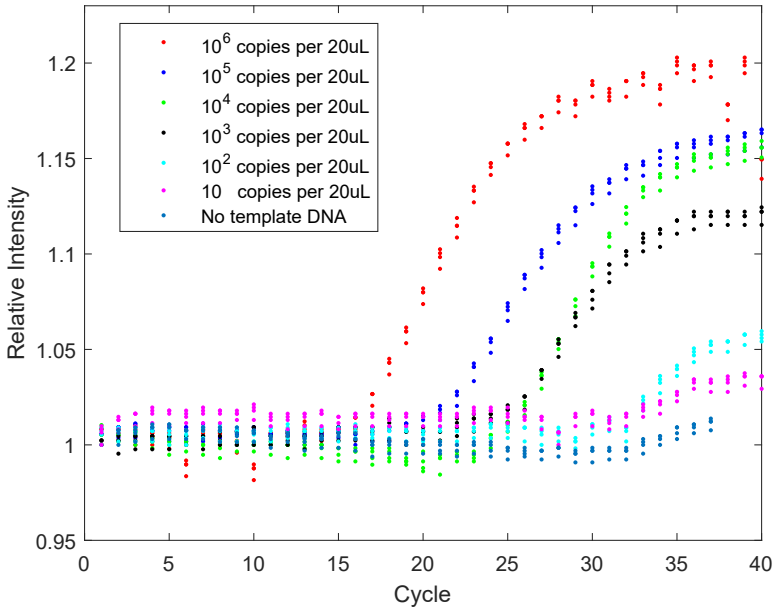

Figure 3.30: UV relative intensity vs cycle plot of different starting DNA concentrations.

Template DNA (Copies/20µL)	10^6	10^5	10^4	10^3	10^2	10
$\boldsymbol{F}$	0.937	0.820	0.785	0.625	0.295	0.191

Table 3.4: Fraction of dNTP converted to dsDNA, with different template DNA concentration.

Chapter 4

Conclusion

4.1 Summary

This thesis gave an overview of PCR and more specifically discussed about the specific components and stages of PCR. It gave an overview of the chemistry, engineering and biology required to perform PCR in both real time and in gel electrophoresis. We discussed the underlying laws of physics involved in direct non-contact heating, variousthermometry techniques, and SISO control systems.

We discovered the inhibition concentration of both PEGylated gold nanorods, non-PEGylated gold nanorods, PEGylated MWCNT and non-PEGylated MWCNT. With the inhibition concentration data, we were able to determine the maximum absorbance per unit length of both nanoparticles to perform PCR. Using non-contact heating and non-contact thermometry, we were able to perform PCR reliably, comparable to that of conventional Peltier blocks PCR. We determined the optimal hold temperatures, and minimum hold time for both the annealing and denaturation stages. Through the optimizations we were able to perform PCR in 7 minutes, running for 35 cycles, with a reaction volume of 20µL.

Most importantly, we were able to demonstrate a simplistic real-time and label-free method to monitor dsDNA production using only a UV LED and UV photodetector, with our relative intensity curve comparable to that of fluorescent intensity curves found in qPCR.

4.2 Further Improvements

4.2.1 Clinical Samples

As we have demonstrated the reliability of our system to perform PCR with purified quantitative CT DNA, the next is to investigate the system's ability to perform PCR of urine samples of patients infected with CT.

4.2.2 Real-Time Detection Characterization

Although the original qualitative goal of having a monitoring system which indicates whether PCR has occurred or not has already been achieve, further experiments can be done to test our system's repeatability and its ability to quantify PCR product.

As clinical samples contain other unknown chemical and biological components, these unknown components could have a non-zero absorption at 260nm which changes under thermal activation. Whether the absorption change of the unknown components occur or not will also need to be investigated.

4.3 Alternatives

As discussed previously other form of electromagnetic heating, from infrared and microwave sources to directly heat liquid can be explored. Although directly heating water from these sources would mean we can no longer tune the absorption for different tubes sizes, this might not be problem since working with a single type of PCR Eppendorf tube is common practice.

Bibliography

[1] Kary B Mullis et al. The unusual origin of the polymerase chain reaction. *Scientific American*, 262(4):56–61, 1990.

[2] Randall K Saiki, Stephen Scharf, Fred Faloona, Kary B Mullis, Glenn T Horn, Henry A Erlich, and Norman Arnheim. Enzymatic amplification of b-globin genomic sequences and restriction site analysis for diagnosis of sickle cell anemia. *Science*, 230(4732):1350–1354, 1985.

[3] Elizabeth Quill. Blood-matching goes genetic. *Science*, 319(5869):1478–1479, 2008.

[4] S Chevillard, Ph Vielh, P Validire, JP Marie, AM Faussat, V Barbu, C Bayle, J Benard, C Bonnal, J Boutonnat, et al. French multicentric evaluation of mdr1 gene expression by rt-pcr in leukemia and solid tumours. standardization of rt-pcr and preliminary comparisons between rt-pcr and immunohistochemistry in solid tumours. *Leukemia (08876924)*, 11(7), 1997.

[5] Rukam S Tomar. *Molecular markers and plant biotechnology*. New India Publishing, 2010.

[6] World Heath Organization. Number of deaths due to hiv/aids estimates by country. http://apps.who.int/gho/data/node.main.623?lang=en, 2017.

[7] SHIRLEY Kwok, DH Mack, KB Mullis, B Poiesz, G Ehrlich, D Blair, A Friedman-Kien, and JJ Sninsky. Identification of human immunodeficiency virus sequences by using in vitro enzymatic amplification and oligomer cleavage detection. *Journal of virology*, 61(5):1690–1694, 1987.

[8] Bernhard Nowak, Theda von Müffling, Sujate Chaunchom, and Jörg Hartung. Salmonella contamination in pigs at slaughter and on the farm: a field study using an antibody elisa test and a pcr technique. *International journal of food microbiology*, 115(3):259–267, 2007.

[9] P-M Jervøe-Storm, M Koltzscher, W Falk, A Dörfler, and S Jepsen. Comparison of culture and real-time pcr for detection and quantification of five putative periodontopathogenic bacteria in subgingival plaque samples. *Journal of clinical periodontology*, 32(7):778–783, 2005.

[10] Khalil Boutaga, Paul HM Savelkoul, Edwin G Winkel, and Arie J van Winkelhoff. Comparison of subgingival bacterial sampling with oral lavage for detection and quantification of periodontal pathogens by real-time polymerase chain reaction. *Journal of periodontology*, 78(1):79–86, 2007.

[11] R Ryan. Fundamental laboratory approaches for biochemistry and biotechnology. *British Journal of Biomedical Science*, 56(2):158, 1999.

[12] Christian D Ahrberg, Bojan Robert Ilic, Andreas Manz, and Pavel Neužil. Handheld real-time pcr device. *Lab on a Chip*, 16(3):586–592, 2016.

[13] Richard R Sinden. *DNA structure and function*. Elsevier, 2012.

[14] Salman Khan. Melting point and thermodynamics of double-stranded dna. https://www.khanacademy.org/test-prep/mcat/physical-sciences-practice/physical-sciences-practice-tut/e/melting-point-and-thermodynamics-of-double-stranded-dna-1g, 2016.

[15] R Bruce Wallace, J Shaffer, RF Murphy, J Bonner, T Hirose, and K Itakura. Hybridization of synthetic oligodeoxyribonucleotides to ϕ x 174 dna: the effect of single base pair mismatch. *Nucleic acids research*, 6(11):3543–3558, 1979.

[16] Chin-Chi Liu and Vince J LiCata. The stability of taq dna polymerase results from a reduced entropic folding penalty; identification of other thermophilic proteins with similar folding thermodynamics. *Proteins: Structure, Function, and Bioinformatics*, 82(5):785–793, 2014.

[17] WJSW Rychlik, WJ Spencer, and RE Rhoads. Optimization of the annealing temperature for dna amplification in vitro. *Nucleic acids research*, 18(21):6409–6412, 1990.

[18] TG Mamedov, Elsje Pienaar, Scott E Whitney, Joel R TerMaat, G Carvill, R Goliath, A Subramanian, and Hendrik J Viljoen. A fundamental study of the pcr amplification of gc-rich dna templates. *Computational biology and chemistry*, 32(6):452–457, 2008.

[19] Harekrushna Sahoo. Fluorescent labeling techniques in biomolecules: a flashback. *Rsc Advances*, 2(18):7017–7029, 2012.

[20] Philippe Quillardet and Maurice Hofnung. Ethidium bromide and safety—readers suggest alternative solutions. *Trends in Genetics*, 4(4):89–90, 1988.

[21] Thermal Fisher Scientific. Quant-it™ picogreen™ dsdna assay kit. https://www.thermofisher.com/order/catalog/product/P11496, 2017.

[22] Ferdinand Friedrich Reuss. Sur un nouvel effet de l'électricité galvanique. *Mem. Soc. Imp. Natur. Moscou*, 2:327–337, 1809.

[23] Marian Smoluchowski. Contribution à la théorie de l'endosmose électrique et de quelques phénomènes corrélatifs. *Pisma Mariana Smoluchowskiego*, 1(1):403–420, 1924.

[24] AFSHIN BEHESHTI. *DNA ELECTROPHORESIS IN AGAROSE GELS: A NEW MOBILITY VS. DNA LENGTH DEPENDENCE*. PhD thesis, THE FLORIDA STATE UNIVERSITY, 600 W College Ave, Tallahassee, FL 32306, USA, 7 2002.

[25] Your Genome. What is gel electrophoresis? https://www.yourgenome.org/facts/what-is-gel-electrophoresis, 2016.

[26] LGC Biosearch Technologies. Detecting signal in qpcr: From dna binding dyes to bhq probes. http://bitesizebio.com/23955/detecting-signal-in-qpcr-from-dna-binding-dyes-to-bhq-probes/, 2015.

[27] Matthew R Hicks, Jarosav Kowałski, and Alison Rodger. Ld spectroscopy of natural and synthetic biomaterials. *Chemical Society Reviews*, 39(9):3380–3393, 2010.

[28] Ross C. Hardison. Working with molecular genetics. http://www.bx.psu.edu/~ross/workmg/workmolecgenethome.html, 2005.

[29] David S Goodsell. The molecular perspective: ultraviolet light and pyrimidine dimers. *The Oncologist*, 6(3):298–299, 2001.

[30] Yun-Long Tsai, Hwa-Tang Thomas Wang, Hsiao-Fen Grace Chang, Chuan-Fu Tsai, Ching-Ko Lin, Ping-Hua Teng, Chen Su, Chien-Chung Jeng, and Pei-Yu Lee. Development of taqman probe-based insulated isothermal pcr (iipcr) for sensitive and specific on-site pathogen detection. *PloS one*, 7(9):e45278, 2012.

[31] Pavel Neuzil, Chunyan Zhang, Juergen Pipper, Sharon Oh, and Lang Zhuo. Ultra fast miniaturized real-time pcr: 40 cycles in less than six minutes. *Nucleic acids research*, 34(11):e77–e77, 2006.

[32] Kai Sun, Akira Yamaguchi, Yutaka Ishida, Shigeki Matsuo, and Hiroaki Misawa. A heater-integrated transparent microchannel chip for continuous-flow pcr. *Sensors and Actuators B: Chemical*, 84(2):283–289, 2002.

[33] Scott Prahl. Optical absorption of water compendium. http://omlc.ogi.edu/spectra/water/abs/index.html, 1998.

[34] Christine Colton James Bolton. *The Ultraviolet Disinfection Handbook*. American Water Works Association, pp. 3–4, 2008.

[35] Nikita Pak, D. Curtis Saunders, Christopher R. Phaneuf, and Craig R. Forest. Plug-and-play, infrared, laser-mediated pcr in a microfluidic chip. *Biomedical Microdevices*, 14(2):427–433, Apr 2012.

[36] Kirsty J. Shaw, Peter T. Docker, John V. Yelland, Charlotte E. Dyer, John Greenman, Gillian M. Greenway, and Stephen J. Haswell. Rapid pcr amplification using a microfluidic device with integrated microwave heating and air impingement cooling. *Lab Chip*, 10:1725–1728, 2010.

[37] R Gans. Über die form ultramikroskopischer silberteilchen. *Annalen der Physik*, 352(10):270–284, 1915.

[38] A Brioude, XC Jiang, and MP Pileni. Optical properties of gold nanorods: Dda simulations supported by experiments. *The Journal of Physical Chemistry B*, 109(27):13138–13142, 2005.

[39] Al-Sayed Abdel-Majied Al-Sherbini. Thermal instability of gold nanorods in micellar solution of water/glycerol mixtures. *Colloids and Surfaces A: Physicochemical and Engineering Aspects*, 246(1):61–69, 2004.

[40] Jorge Pérez-Juste, Luis M Liz-Marzán, Steven Carnie, Derek YC Chan, and Paul Mulvaney. Electric-field-directed growth of gold nanorods in aqueous surfactant solutions. *Advanced Functional Materials*, 14(6):571–579, 2004.

[41] Kyoungweon Park, Sushmita Biswas, Sushil Kanel, Dhriti Nepal, and Richard A Vaia. Engineering the optical properties of gold nanorods: independent tuning of surface plasmon energy, extinction coefficient, and scattering cross section. *The Journal of Physical Chemistry C*, 118(11):5918–5926, 2014.

[42] Hugh H Richardson, Michael T Carlson, Peter J Tandler, Pedro Hernandez, and Alexander O Govorov. Experimental and theoretical studies of light-to-heat conversion and collective heating effects in metal nanoparticle solutions. *Nano letters*, 9(3):1139–1146, 2009.

[43] Matthew Charles Stensberg, Qingshan Wei, Eric Scott McLamore, David Marshall Porterfield, Alexander Wei, and María Soledad Sepúlveda. Toxicological studies on silver nanoparticles: challenges and opportunities in assessment, monitoring and imaging. *Nanomedicine*, 6(5):879–898, 2011.

[44] Seung S Lee, Philip JR Roche, Paresa N Giannopoulos, Elliot J Mitmaker, Michael Tamilia, Miltiadis Paliouras, and Mark A Trifiro. Prostate-specific membrane antigen–directed nanoparticle targeting for extreme nearfield ablation of prostate cancer cells. *Tumor Biology*, 39(3):1010428317695943, 2017.

[45] T. J. Quinn. *Temperature*. London: Academic Press, 1983.

[46] Donald E Kirk. *Optimal control theory: an introduction*. Courier Corporation, 2012.

[47] Daniel Wüstner, Tanja Christensen, Lukasz M Solanko, and Daniel Sage. Photobleaching kinetics and time-integrated emission of fluorescent probes in cellular membranes. *Molecules*, 19(8):11096–11130, 2014.